

## ABSTRACT

JIAN, WEIWEI. Ultrastrong Mg Alloy via Nano-Spaced Stacking Faults. (Under the direction of Prof. Yuntian T. Zhu and Prof. Carl C. Koch).

Magnesium and its alloys have attracted extensive attention in recent years due to their abundance, low-density, good castability and recyclability. However, the application of Mg alloys has been substantially hindered by their relatively low strengths and limited ductility at room temperature. Outside of traditional precipitation control, Mg-alloy strengthening typically relies on two general approaches: non-traditional, esoteric processing and grain refinement. Here in this research, we processed a Mg-8.5Gd-2.3Y-1.8Ag-0.4Zr (wt.%) via conventional technique (hot-rolling at 450°C) with thickness reduction up to 88%. The main contents of this research, as well as the novelties, are discussed in the following ways.

Firstly, we reported a new mechanism for producing ultrahigh strengths (yield strength: ~575 MPa, ultimate strength: ~600 MPa) and maintaining moderate ductility (uniform elongation: ~ 3% to 4%) in hot rolled Mg-alloy with relatively large grain sizes (13  $\mu\text{m}$ ). TEM studies show that a high density of nano-spaced SFs are the main defects inside of the grains and their density increased as rolling thickness reduction increased. The strength of the processed Mg alloy was found to increase as the mean spacing between adjacent SFs decreased. Nano-spaced SFs were found to be very effective in impeding the movement of dislocations and retaining strain hardening. Activation of non-basal dislocations during tensile testing accounts for the detected moderate ductility, in addition to the capability of retaining strain hardening.

Secondly, we predicted and calculated contributions from different strengthening mechanisms for the ultrahigh strength of hot rolled Mg alloy including solid solution, grain refinement, precipitation and texture evolution. The results showed that grain boundary

strengthening, solid solution hardening, precipitates hardening and strong texture strengthening totally contribute 249.8 MPa to 278.5 MPa for the yield strength (~575MPa) of 88% rolled Mg alloy. In other words, the nano-spaced SFs strengthening mechanism was the main strengthening factor, which solely contributed 326.2 MPa to 296.5 MPa, around 50% of the total yield strength.

Finally, the model of interactions between basal SFs and basal  $\langle a \rangle$  dislocations and non basal  $\langle c+a \rangle$  dislocations were established for the first time in Mg alloy. The model showed that the strengthening was proportional to the reciprocal of the SF spacing for both types of interactions between dislocations and SFs. Therefore, decreasing the SF spacing can increase interaction force which served as a barrier for a dislocation to move, and consequently improved the macroscopic strength of materials.

In summary, introducing nano-spaced SFs in Mg alloy can tremendously impede the movement of dislocations and retain strain hardening. It is expected that optimization of approaches that introduce a high density of nano-spaced SFs will enable other Mg-alloys with concurrent high strength and good ductility.

© Copyright 2012 by Weiwei Jian

All Rights Reserved

Ultrastrong Mg Alloy via Nano-Spaced Stacking Faults

by  
Weiwei Jian

A dissertation submitted to the Graduate Faculty of  
North Carolina State University  
in partial fulfillment of the  
requirements for the degree of  
Doctor of Philosophy

Materials Science and Engineering

Raleigh, North Carolina

2012

APPROVED BY:

---

Dr. Yuantian Zhu  
Committee Co-Chair

---

Dr. Carl Koch  
Committee Co-chair

---

Dr. Ronald Scattergood  
Committee Member

---

Dr. Mike Rigsbee  
Committee Member

---

Dr. Suveen Mathaudhu  
Committee Member

## **DEDICATION**

I dedicate this dissertation

to my parents, Huixian Jiang and Changyou Jian

for their unconditional support whenever I need them.

To my grandmother, Xingyu Wu, who will be in my memory forever.

## **BIOGRAPHY**

Weiwei Jian was born in Jingmen City at Hubei Province of China on July 20<sup>th</sup>, 1982. After eighteen years living and studying in his small but beautiful hometown, he went to pursue his Bachelor Degree in Mechanical Engineering in South China University of Technology (SCUT) at Guangzhou, China. There he was a graduate student majoring in Materials Processing Engineering. He received his master degree in 2008 under the supervision of Dr. Zhixin Kang, for his research in thermal-mechanical processing (equal channel angular extrusion and multi-directional forging) of Mg alloys and investigating microstructure and mechanical property relationship. Encouraged by Dr. Kang at SCUT, Weiwei then decided to join the Department of Materials Science and Engineering at North Carolina State University (NCSU) under the supervision of Dr. Yuntian Zhu and Dr. Carl Koch. Since August 2008, Weiwei spent most of his research time and effort on exploiting a new strengthening mechanism for improving the strength, without severe loss of ductility, of Mg alloys. With generous financial support from US Army Research Office (ARO) and US Army Research Lab (ARL), Weiwei made some breakthroughs in this area, which are the main contents of this dissertation.

## ACKNOWLEDGMENTS

First I would like to thank my co-supervisors, Dr. Y.T. Zhu and Dr. C.C. Koch, for their endless encouragement and patience to let me try different experiments on various materials (obviously most of my experiments are failed) in my research. Without their support and guidance, I would not be where I am today.

I would also like to express my appreciation to Dr. S.N. Mathaudhu (ARO, USA) for his guidance, and his supervision of my research and publications. He is always willing to share his challenging but practical ideas with me.

I also wish to acknowledge my former supervisor, Dr. Z.X. Kang (SCUT, China), who was my first mentor in academia, taught me how to research and encouraged me to pursue a professional career in academia.

During my past four years at NCSU, I was lucky that I was able to get help and collaborate with Dr. R.O. Scattergood, Dr. M. Rigsbee, Dr. H. Conrad, Dr. J. Kasichainula, Dr. L. Reynolds Jr., Dr. G.M. Cheng, Dr. X. Wang, Dr. M.H.Tsai, Dr. K. Youssef, Dr. H. Bahmanpour, Dr. M. Atwater, Mr. X.K. Zhu, Ms. W. Piyawit, Mr. W.Z. Xu, Mr. H. Yuan, Mr. J. Wang, Ms. Y.C. Yuan, Ms. J.M.Tao Mr. X.L. Ma, Mr. F. Wu, Mr. J. Moore (NCSU), Dr. Q.M. Wei (UNC-Charlotte), Dr. L.J. Kecskes and Dr. K. Darling (ARL, USA), Dr. J.H. Jiang, Dr. A.B. Ma (Hohai University, China), Dr. V.S. Sarma (IIT, India), Dr. L.Z. Ouyang (SCUT), Dr. S. Mula (NIT, India). Thank you all!

I would also like to thank Dr. David Stepp (ARO, USA) for his administration of my research projects and financial support.

Finally, I would like to give special thanks to my fiancée Zhiying (Emmy) Yu. She knows why I spend most of my weekends in the lab.

## TABLE OF CONTENTS

<b>LIST OF TABLES.....</b>	<b>ix</b>
<b>LIST OF FIGURES.....</b>	<b>x</b>
<b>CHAPTER 1: Introduction.....</b>	<b>1</b>
1.1 Mg Alloy and Its Potential Applications.....	1
1.2 Deformation Mechanisms of Magnesium Alloys.....	2
1.2.1 Dislocation Motion.....	2
1.2.2 Stacking Faults.....	11
1.2.3 Deformation Twinning .....	13
1.3 Strengthening Strategies of Magnesium Alloys.....	18
1.3.1 Solid Solution Strengthening .....	18
1.3.2 Precipitate Hardening.....	19
1.3.3 Strain Hardening .....	21
1.3.4 Grain Boundary Strengthening .....	22
REFERENCES.....	23
<b>CHAPTER 2: Experiments .....</b>	<b>27</b>
REFERENCES.....	29
<b>CHAPTER 3: Ultrastrong Mg-Alloy via Nano-Spaced Stacking Faults.....</b>	<b>30</b>

3.1 Introduction.....	30
3.2 Experimental Procedures.....	31
3.3 Results and Discussion.....	32
3.4 Summary.....	40
REFERENCES.....	41

**CHAPTER 4: Investigation of Strengthening Mechanisms in an Ultrastrong Mg Alloy**

<b>Processed by Hot Rolling.....</b>	<b>48</b>
4.1 Introduction.....	48
4.2 Prediction and Calculation of Various Strengthening Contribution.....	49
4.2.1 Grain Boundary Strengthening, $\sigma_1$ .....	49
4.2.2 Solid Solution Hardening, $\sigma_2$ .....	50
4.2.3 Precipitates Hardening, $\sigma_3$ .....	52
4.2.3.1 Dislocation-particle Interaction by Orowan Stress.....	52
4.2.3.2 Dislocation Generation due to a Difference in Thermal Expansion.....	53
4.2.3.3 Dislocation Generation Required Geometrically during Deformation....	54
4.2.4 Strong Texture Strengthening, $\sigma_4$ .....	57
4.3 Summary.....	57
REFERENCES.....	59

**CHAPTER 5: Strengthening Mechanism of Mg alloy by Nano-Spaced SFs..... 61**

5.1 Introduction.....	61
-----------------------	----

5.2 Identification of Dislocations Activated during Tensile Test .....	63
5.3 Interaction between SFs and $\langle a \rangle$ Dislocation on Basal Plane .....	65
5.4 $\langle c \rangle$ Dislocation and $\langle c+a \rangle$ Dislocation Interact with SFs .....	71
5.5 Summary.....	79
REFERENCES.....	80
<b>CHAPTER 6: Conclusions and Future Work .....</b>	<b>82</b>
6.1 Conclusions.....	82
6.2 Future Work .....	83
<b>APPENDIX .....</b>	<b>85</b>
Appendix A: Solution Treatment.....	86
Appendix B: Calculations of the Diameter and Volume Fraction of Precipitate.....	90

## LIST OF TABLES

<b>Table 1.1</b> Specific names of a number of planes in hexagonal lattice.....	9
<b>Table 1.2</b> The $c/a$ ratio and preferred slip planes in common hcp metals at 300 K .....	9
<b>Table 1.3</b> The possible slip planes and associated dislocations in hcp metals .....	16
<b>Table 4.1</b> EDS result of the concentration of the solutes (at.%) in matrix of 450°C 88% rolled Mg-8.5Gd-2.3Y-2.0Ag-0.4Zr sample .....	52
<b>Table 5.1</b> Maximum interaction force between $\langle c \rangle$ dislocation and SFs at few selected $x$ values .....	76
<b>Table A.1</b> The image pixels of 18 precipitates in Figure A.3.....	92

## LIST OF FIGURES

<b>Figure 1.1</b> Various Mg automobile parts used in European automobile industry.....	3
<b>Figure 1.2</b> Illustration of lattice structure of (a) hcp in regardless of $c/a$ ration, (b) fcc and (c) bcc .....	4
<b>Figure 1.3</b> Illustration of slip of a pure edge dislocation .....	5
<b>Figure 1.4</b> Illustration shows how the perfect dislocation dissociated into partial dislocations .....	7
<b>Figure 1.5</b> Thompson's Tetrahedron in fcc lattice .....	10
<b>Figure 1.6</b> Illustration of the shears associated with (a) twinning and (b) slip .....	17
<b>Figure 2.1</b> Rolling machine used in current experiment.....	28
<b>Figure 3.1</b> Engineering stress-strain curves of Mg-8.5Gd-2.3Y-1.8Ag-0.4Zr (wt.%) samples under T4 treatment and hot rolling with different thickness reductions (marked by the curves).....	33

**Figure 3.2** Summary of room temperature tensile yield strength and uniform elongation of previous reports and our current work. The criteria used to summarize and reproduce this figure are (1) only room temperature uniaxial tensile test results were included, (2) the gauge length of tensile test sample was larger than 5 mm, and (3) the stress-strain curve must be indicated in the individual report in order to reproduce the uniform elongation. The reference number is by the data point..... 34

**Figure 3.3** TEM images of Mg-8.5Gd-2.3Y-1.8Ag-0.4Zr (wt.%) alloy samples with various rolling thickness reductions: (a) 50%,  $d=55$  nm, (b) 70%,  $d=25$  nm and (c) 88%,  $d=16$  nm. Image (d) is the SAD pattern of the 70% rolled sample in which the streaking verifies the basal plane SFs. .... 36

**Figure 3.4** Yield strength vs the reciprocal of mean spacing between SFs of rolled samples with different thickness reduction. The number by each data point indicates the thickness reduction by hot rolling..... 37

**Figure 3.5** TEM images of 88% hot rolled sample after tensile test. (a) Fragments of SFs cut by the dislocations. (b) The yellow dash line indicates SFs and white circles mark the fragmented SFs with few atomic layer spacing steps. .... 39

**Figure 4.1** OM images of Mg-8.5Gd-2.3Y-2.0Ag-0.4Zr alloy: (a) as-cast, (b) T4 treated and (c) T4 treated+450 °C 88% hot rolled ..... 51

**Figure 4.2** TEM image show the distribution of precipitates in 88% hot rolled Mg-8.5Gd-2.3Y-2.0Ag-0.4Zr sample. Non-spherical precipitates are marked by white arrows ..... 55

**Figure 4.3** TEM image shows dislocations trapped around precipitates..... 56

**Figure 4.4** XRD patterns of as quenched and hot rolled samples shows the texture evolution ..... 58

**Figure 5.1** TEM image of Mg-8.5Gd-2.3Y-1.8Ag-0.4Zr (wt.%) alloy samples: (a) 88% hot rolled before tensile test,(b) 88% hot rolled after tensile test, (c) and (d) two-beam bright field images with different g vectors indicated the white arrows..... 64

**Figure 5.2** Schematic illustration of (a) the interaction of  $\langle a \rangle$  dislocation with two adjacent stacking faults, (b) and (c) show how to establish the co-ordinate system for stress calculation using Peach-Koehler equation..... 69

**Figure 5.3** Schematic illustration of (a) the interaction of  $\langle a \rangle$  dislocation with two adjacent stacking faults, (b) and (c) show how to establish the co-ordinate system for stress calculation using Peach-Koehler equation..... 73

**Figure 5.4** Schematic illustration of non basal slip system ..... 74

**Figure 5.5** Configuration of the  $\langle c \rangle$  dislocation interact with two adjacent SFs ..... 74

**Figure 5.6** Schematical illustration for (a)  $\langle c+a \rangle$  dislocation moves close to a stacking fault and (b)  $\langle c+a \rangle$  dislocation cut through a SF and leave a step on the SF..... 78

**Figure A.1** OM images of Mg-8.5Gd-2.3Y-2.0Ag-0.4Zr alloy solution treated at 520 °C for 10 hours and then quenched in different media: (a) 20 °C water, (b) engine oil..... 88

**Figure A.2** OM images of Mg-8.5Gd-2.3Y-2.0Ag-0.4Zr alloy solution treated at different temperatures for variant time and then quenched in different media: (a) 500 °C for 10 hours, quenched in 20 °C water, (b) 500 °C for 10 hours, quenched in room temperature silicon oil and (c) 500 °C for 12 hours, quenched in room temperature silicon oil. .... 89

**Figure A.3** The typical precipitates in 88% rolled Mg-8.5Gd-2.3Y-1.8Ag-0.4Zr (wt.%) alloy samples..... 91

## CHAPTER 1: Introduction

### 1.1 Mg Alloy and Its Potential Applications

Magnesium was discovered in the early nineteenth century. Mg has abundant resources on the earth, which are usually in the form of magnesite, dolomite and other minerals. Mg can be obtained by electrolysis of melted magnesium chloride ( $\text{MgCl}_2$ ) derived from brines, wells and sea water. Magnesium is the third metallic element in the periodic table and has the lowest density of any of the structural metals (1.74 g/cc). With its low density, magnesium is 35% lighter than aluminum and 78% lighter than steel. This characteristic triggers extensive interest in researching and application of Mg alloys in the automobile and aircraft industries. In fact, there are already some successful applications of Mg alloys in the European automobile industry in items such as steering wheels, steering column parts, instruments panels, seats, gear boxes, air intake systems, stretchers, gearbox housings and tank covers, all of which are illustrated in Figure 1.1. However, the applications of Mg alloys so far are mainly confined to die casting components.

The lattice structure of Mg is hexagonal close-packed (hcp) which has low symmetry compared with face-centered cubic (fcc) and body-centered cubic (bcc) as shown in Figure 1.2. As we will discuss in the next sub-section, the activated slip systems of the hcp structure are less than those of fcc and bcc structures at room temperature. For this reason, as well as its relatively low melting point, Mg usually suffers from relatively low strength, ductility, and formability which can greatly limit the application of Mg alloys.

A number of studies in recent years have attempted to increase the strength and ductility of Mg-based alloys by grain refinement, addition of dispersoids or introducing fine and

uniformly distributed precipitates, or changes in texture. With a nanocrystalline matrix, the yield strength of Mg can be increased from about 120 MPa for commercial extruded Mg to about 180 MPa for nanocrystalline Mg with a 45 nm grain size [1]. To date, the yield strength of the most commercial Mg alloy falls in the range of ~100 MPa to 250 MPa [2]. Compared with other structural materials, such as Al alloys and steels, it seems Mg alloys still have room for improving mechanical properties.

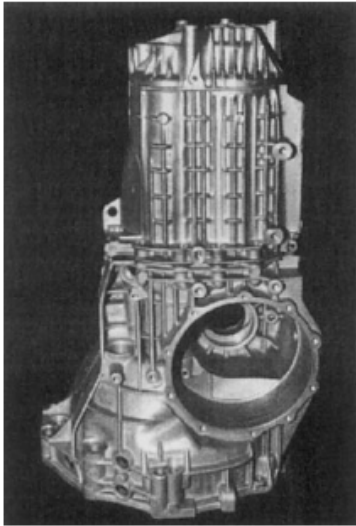
The mechanical properties of metallic materials are controlled by microstructures and deformation mechanisms. Thus, understanding the deformation mechanisms and tailoring the appropriate microstructure will be crucial for finding strategies to improve the mechanical properties. In the following sub-sections, the deformation mechanisms and strengthening strategies in Mg alloys will be discussed.

## 1.2 Deformation Mechanisms of Magnesium Alloys

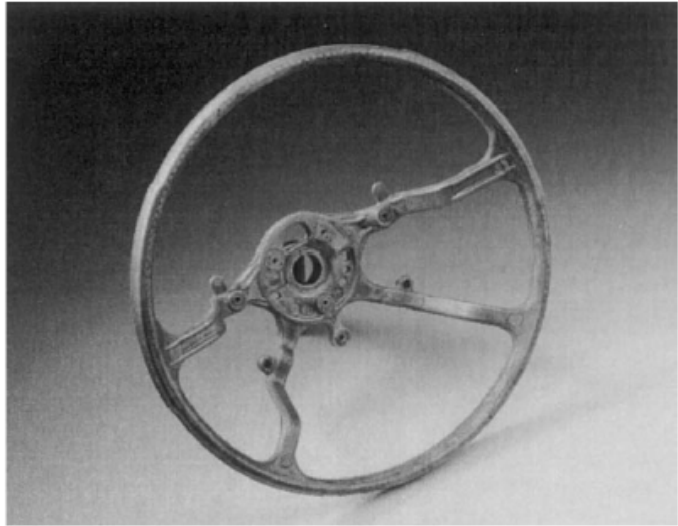
### 1.2.1 Dislocation Motion

There are two basic types of dislocation motion: slip and climb. Slip is a conservation movement occurring on slip planes, which contains both dislocation line and Burgers vector, in the slip directions. At low temperature, the non-equilibrium concentration of point defects is not sufficient, due to the restriction of the diffusion process, such that the motion of dislocation is confined almost entirely to slip [4]. Figure 1.3 illustrates a pure edge dislocation slipping on the slip plane. Once the dislocation slips onto the surface of crystalline solids, a step which equals to the magnitude of Burgers vector will be left, as shown in Fig. 3. So, the plastic deformation in crystalline materials is mainly manifested to

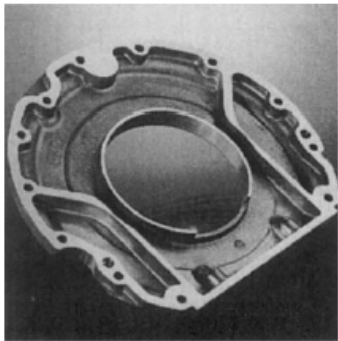
slip of many dislocations on one slip plane over another. This principle is also applicable to pure edge dislocations and mixed dislocations [4].



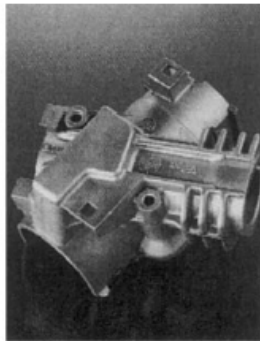
Gear Box Housing



Steering Wheel Frame



Sealing Flange



Steering Column Lock

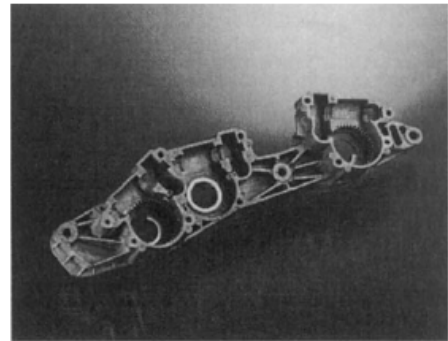


**Figure 1.1** Various Mg automobile parts used in European automobile industry [3].

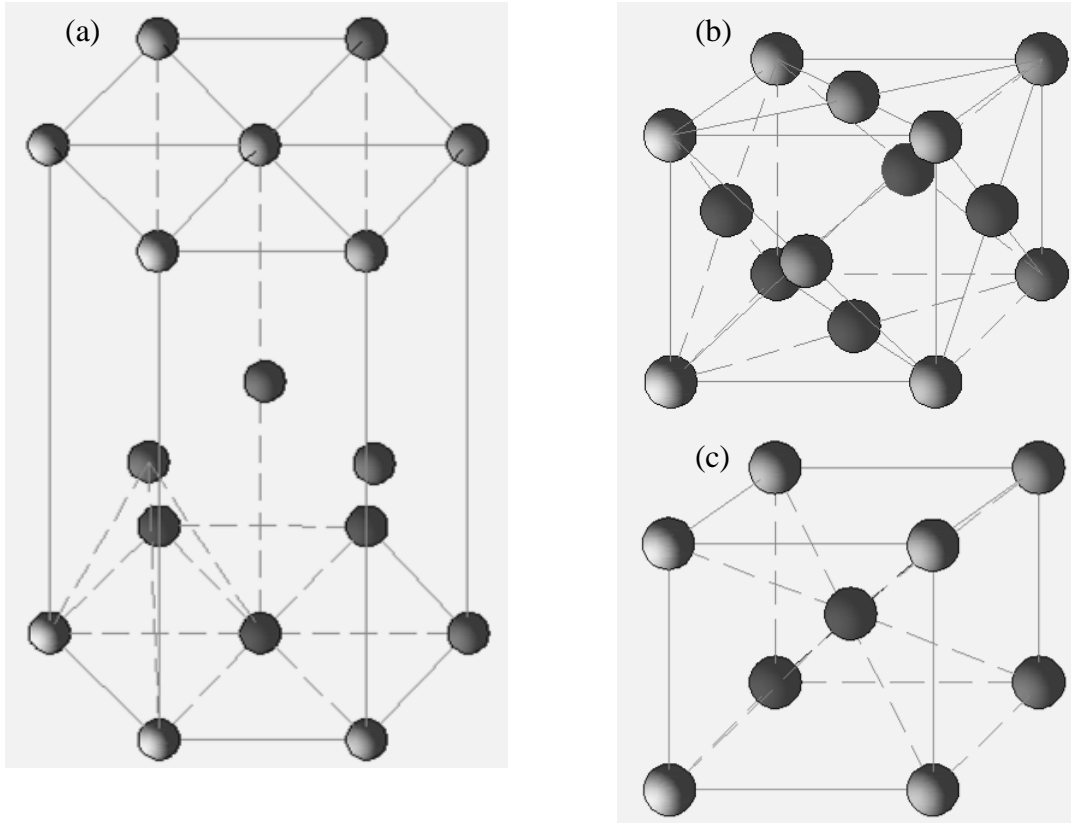


**Figure 1.2** Illustration of lattice structure of (a) hcp in regardless of  $c/a$  ratio, (b) fcc and (c) bcc.

Dislocation climb is the motion on the surface perpendicular to the slip plane and thus normal to the Burgers vector. The edge dislocation climbs up and down by removing or adding one atom on the extra half plane. In real crystalline solids, this process is achieved by diffusion of point defects such as vacancies and/or interstitial atoms. This diffusion-controlled process usually happens at relatively higher temperatures [4].

Face-centered cubic, body-centered cubic and hexagonal-close packed structures are three typical lattice structures of structural metallic materials. Dislocations in these metals usually slip on close packed planes along close packed directions (except for bcc metals). Here, the discussion will be confined to fcc and hcp metals because: (1) many common metals such as Cu, Al, Ag, Au and Ni are fcc structures and their slip planes and directions are well-defined. (2) The slip lines in bcc metals are often curved and ill-defined and the slip planes varies with composition, crystal orientation, temperature and strain rate and (3) Mg alloys with hcp structure are the targeted materials in this research.

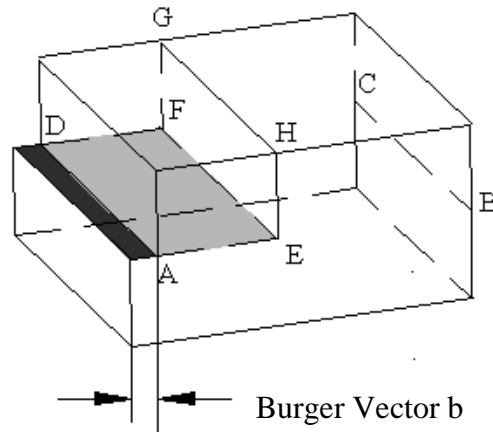


**Figure 1.3** Illustration of slip of a pure edge dislocation.

In fcc metals, the slip system are families of  $\{111\} \langle 110 \rangle$  where the slip planes are four  $\{111\}$  close-packed atomic planes and the slip directions are three  $\langle 110 \rangle$  close-packed directions on each slip plane. Other slip systems were rarely observed, at least at the room temperature. The stacking sequence of the  $\{111\}$  plane in fcc structures is ABCABCABC... which can be illustrated by hard spheres model as shown in Fig. 4. Here

the atoms on the first (111) plane locate in the A position and the atoms on the second successive (111) plane can rest in either B or C position which are crystallographically equal to each other. For simplicity, we assign the atoms on the second (111) plane to sit in the B positions. The difference of stacking sequence between fcc and hcp metals is attributed to the location of the atoms on the third (111) plane. If atoms locate in C positions, the stacking sequence is ABCABC... which is the fcc structure. However, when atoms locate on the A position again, the stacking sequence become ABAB... This is the stacking sequence of the basal plane in hcp metals.

In Figure 1.4, it can be seen that slip of the second (111) plane (B layer of atoms) from one B site to the next B site, as indicated by the vector  $\mathbf{b}_1$ , will cross the bumper of atom in A site. This process is energetically unfavorable. Instead, B layer of atoms will first move through to valley between the two A atoms to C site ( $\mathbf{b}_2$ ) and then to the next B site via a second valley ( $\mathbf{b}_3$ ). In other word, the Burgers vector  $\mathbf{b}_1$  can split up or dissociate into two vectors  $\mathbf{b}_2$  and  $\mathbf{b}_3$  according to the reaction of  $b_1 \rightarrow b_2 + b_3$ . Vector  $\mathbf{b}_1$  is called the perfect vector and  $\mathbf{b}_2$  and  $\mathbf{b}_3$  are called Shockley partial dislocations.

In fcc structures, the Shockley partial dislocation vector is  $\mathbf{b}_2 = \mathbf{b}_3 = \mathbf{a}/6\langle 112 \rangle$  and the perfect dislocation vector is  $\mathbf{b}_1 = \mathbf{a}/2\langle 110 \rangle$ . The energy of a dislocation is proportional to the square of the magnitude of its Burgers vector  $b^2$ . The energy of a perfect dislocation is proportional to  $b^2 = a^2/2$  and the total energy of the two partial dislocations is proportional to  $b^2 = a^2/6 + a^2/6 = a^2/3$  which is less than  $a^2/2$ . So dissociation of perfect dislocation into two Shockley partials is energetically favorable.

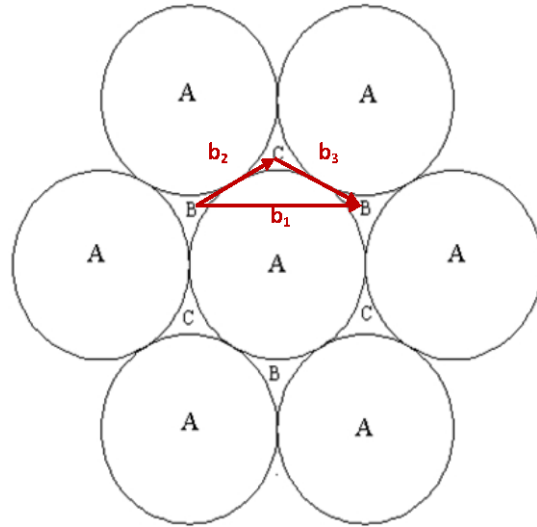


**Figure 1.4** Illustration shows how the perfect dislocation dissociated into partial dislocations.

As mentioned in the above section, there are four equivalent (111) planes and three equivalent [110] directions on each (111) planes in fcc structure. These 12 slip systems seem make the work much more complex when analyzing the perfect dislocations and Shockley partials. Under these circumstances, Thompson's Tetrahedron is introduced to describe all the important dislocations and dislocations reactions in fcc metals as shown in Figure 1.5 [4]. The principles of constructing a tetrahedron are that the four equivalent (111) planes lie parallel to the four faces of a regular tetrahedron and the edges of the tetrahedron are parallel to the  $\langle 110 \rangle$  slip directions. A tetrahedron can be formed by join A, B, C sites, the center of three perpendicular planes, and D site, a corner site of fcc lattice. The corners of the tetrahedron are denoted by A, B, C, D and the mid-points of the opposite faces by  $\alpha$ ,  $\beta$ ,  $\gamma$  and  $\delta$  [4]. The edge of the tetrahedron such as **AC**, **BC**, **CA**, etc., can present both the direction

and magnitude of the Burgers vectors  $\frac{1}{2}\langle 110 \rangle$  of perfect dislocations in FCC structure. The Shockley partials Burgers vector  $\frac{1}{6}\langle 112 \rangle$  can be defined by the line from the corner to the center of a face, such as  $\mathbf{A}\beta$ ,  $\mathbf{A}\gamma$ , etc. Once the perfect dislocation dissociates into a pair of Shockley partials, a stacking fault ribbon will form between the partials.

In hcp metals, dislocation behavior becomes much more complex than dislocation behavior for fcc metals since the crystal symmetry, the nature of interatomic bonding, and the number of atoms in the lattice are different. Before discussion of the slip planes of hcp metals, a number of planes in hexagonal lattice need to be specified, as seen in Table 1.1. Prismatic and pyramidal planes are also referred to non-basal planes. At room temperature, the active slip planes of hcp metals likely depend on the  $c/a$  ration. The  $c/a$  ratio and preferred slip planes in common hcp metals are shown in Table 1.2.

For describing the Burgers vectors of dislocations in hcp metals, it is more convenient to use the primitive vectors  $\mathbf{a}$  and  $\mathbf{c}$  of the hexagonal lattice, as shown in Table 1.3. A translation vector in a close-packed direction will be called “a vector of type  $\langle \mathbf{a} \rangle$ ”. A translation vector along a  $\langle -1-123 \rangle$  direction will be called “a vector of type  $\langle \mathbf{a}+\mathbf{c} \rangle$ ” [6]. The planes and directions that are considered as possible slip planes are summarized in Table 1.3.

The  $\langle \mathbf{a} \rangle$  Burgers vectors on basal plane and first-order prismatic plane only provide four independent slip systems. All the slip systems on pyramidal plane with  $\langle \mathbf{a} \rangle$  Burgers vectors are crystallographically equivalent to the combined four independent modes by cross slip between basal and prismatic slip systems with  $\langle \mathbf{a} \rangle$  Burgers vectors [6]. Thus, there will be at most four independent slip systems with  $\langle \mathbf{a} \rangle$  Burgers vector during deformation. According to the von Mises criterion, a polycrystalline material needs to activate five

independent slip systems to undergo a general homogenous deformation without producing cracks [7]. Therefore, the activation of slip system with  $\langle \mathbf{a}+\mathbf{c} \rangle$  Burgers vector on pyramidal plane combined with the four slip systems ( $\langle \mathbf{a} \rangle$  Burgers vectors on basal plane and first-order prismatic plane) can provide five independent slip systems to fulfill the von Mises criterion [8].

**Table 1.1** Specific names of a number of planes in hexagonal lattice [4].

<b>Name of plane</b>	<b>Miller-Bravais indices</b>
<b>Basal plane</b>	<b>(0001)</b>
<b>Prism plane: first order</b>	<b>(1-100) (-1100), etc.</b>
<b>Prism plane: second order</b>	<b>(11-20) (-2110), etc.</b>
<b>Pyramidal plane: first order</b>	<b>(10-11) (-1011), etc.</b>
<b>Pyramidal plane: second order</b>	<b>(11-22) (-1-122), etc.</b>

**Table 1.2** The  $c/a$  ratio and preferred slip planes in common hcp metals at 300 K [4,5, 6].

<b>Metal</b>	<b>Be</b>	<b>Ti</b>	<b>Zr</b>	<b>Mg</b>	<b>Co</b>	<b>Zn</b>	<b>Cd</b>
<b><math>c/a</math> ratio</b>	<b>1.568</b>	<b>1.587</b>	<b>1.593</b>	<b>1.623</b>	<b>1.628</b>	<b>1.856</b>	<b>1.886</b>
<b>Preferred slip</b>	<b>basal</b>	<b>prism</b>	<b>Prism</b>	<b>basal</b>	<b>basal</b>	<b>basal</b>	<b>basal</b>
<b>Plane for <math>b=a</math></b>	<b>(0001)</b>	<b>{10-10}</b>	<b>{10-10}</b>	<b>(0001)</b>	<b>(0001)</b>	<b>(0001)</b>	<b>(0001)</b>

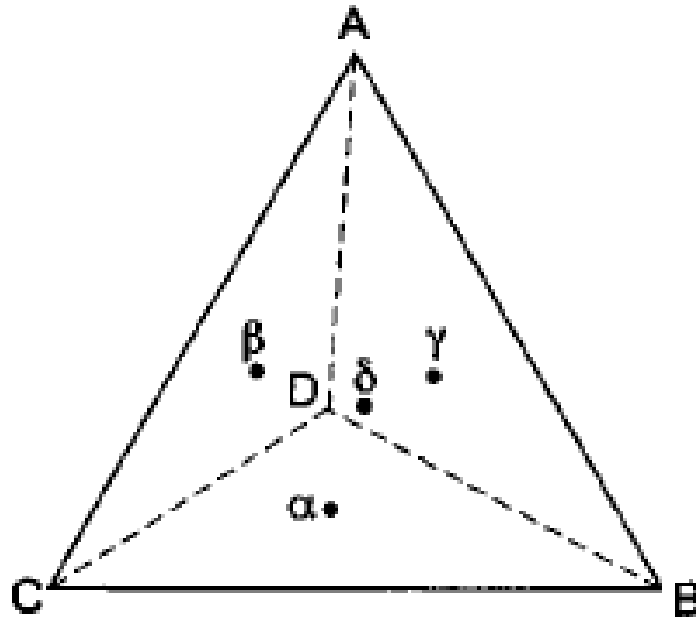


**Figure 1.5** Thompson's Tetrahedron in fcc lattice [4].

Deformation of Mg by dislocation slip is essentially limited to the basal plane (0001) with  $\langle a \rangle$  Burgers vector which was confirmed by Roberts and Wonsiewicz and Backofen in the 1950s and 1960s [9, 10]. Other slip mechanisms observed include the slip of  $\langle a \rangle$  type of dislocations on prismatic  $\{10\text{-}10\}$  and pyramidal  $\{10\text{-}11\}$  planes [11-14]. These non-basal slip systems were only activated at relatively high temperatures and, thus, were widely held responsible for the good elevated temperature ductility of Mg and its alloys. Only dislocations with non-basal Burgers vector will accommodate deformation along the c-axis which completes the requirement of five independent slip modes. It was until the early 1970s

when the transmission electron microscopy (TEM) was available for dislocation observation that the  $\langle \mathbf{a}+\mathbf{c} \rangle$  type of dislocation ( $\mathbf{b}=\frac{1}{3}\langle 11-23 \rangle$ ) were confirmed [15], which slips on the first-order pyramidal plane and provides the fifth independent slip system that fulfill the von Mises criterion.

### 1.2.2 Stacking Faults

As discussed in section 1.2.1, the perfect dislocation  $\mathbf{b}_1$  can dissociate into two Shockley partials with Burgers vectors of  $\mathbf{b}_2$  and  $\mathbf{b}_3$  on the close-packed plane. These two Shockley partials were not necessary to be immediately adjacent to each other. If they separate there will be a ribbon of stacking faults between them.

A stacking fault is a planar defect where the regular sequence has been interrupted. Stacking faults are not expected in planes with ABABAB... sequences in bcc or fcc metals since there is no alternative site for an A layer resting on a B layer. However, there are two possible sites of one layer resting on another for ABCABC... or ABAB... stacking of the close-packed planes in close-packed structures. Intrinsic faults can be regarded as removing part of a C layer which results in a break in the stacking sequence. Actually, this type of stacking fault is created by slipping of the Shockley partial  $\frac{1}{6}\langle 112 \rangle$  on the close-packed plane  $\{111\}$ . The motion of Shockley partial can move B layer to the position of C layer and C layer above initial B layer to the position of A layer and so on. An extrinsic fault is formed by inserting one close-packed  $\{111\}$  layer of atoms such that the stacking sequence becomes ABCABACABC... This type of fault is bounded by the Frank partial dislocations with Burgers vector of  $\mathbf{b}=\frac{1}{3}\langle 111 \rangle$  which is equal to the change in spacing produced by one close-packed layer. Since the Burgers vector of Frank partial dislocation is normal to the

close-packed slip plane  $\{111\}$ , the Frank partial can only move by climb. Such a dislocation is said to be sessile, unlike the glissile Shockley partial.

In hcp metals, the stacking sequence of close-packed plane  $\{0001\}$  is ABABAB... Interruption of this stacking sequence can result in three types of basal-plane faults, two intrinsic,  $I_1$  and  $I_2$ , and an extrinsic  $E$  [4]. Fault  $I_1$  is formed by removing a basal layer, such as the A layer, which results in the atoms of the B layer above the fault sitting directly adjacent to the B layer below the fault. This configuration has very high energy which can be reduced by slip of  $1/3\langle 10\bar{1}0 \rangle$  of the atomic layer above this fault:



If the A layer slips of  $1/3\langle 10\bar{1}0 \rangle$  to the site for C layer, fault  $I_2$  will be formed in a perfect crystal:



Fault  $E$  is produced by inserting an extra plane into the perfect crystal which gives the fault sequence:



The fcc close-packed stacking sequences, ABC or BCA or CAB, are introduced in the hcp crystal and these faults have a characteristic stacking-fault energy  $\gamma$  (SFE). The main contribution of  $\gamma$  arises from changes in the second-neighbour sequences of the planes. As shown above, there is one ABC stacking sequence in  $I_1$ , two (ABC and BCA) for  $I_2$  and three (ABC, BCA and CAB) for  $E$  and so to a first approximation  $\gamma_E \approx 3/2\gamma_{I_2} \approx \gamma_{I_1}$  [4]. When a stacking fault is formed in the crystal, the SFE provides a force to pull the dissociated dislocations together, while partial dislocations have the tendency to repulse each other. An

equilibrium separation is therefore established when the attractive and repulsive forces balance according to the equation:  $d = Gb^2 / 4\pi \gamma$ . So the dissociation of dislocation into partials and consequent formation of stacking faults are related to the stacking fault energy of the crystals.

### 1.2.3 Deformation Twinning

Twinning is another deformation mechanism in plastic deformation of metals. The lattice of twin is a mirror image or reflection of the parent lattice in the twinning plane. When a crystal is twinned, there is no change in crystal structure but merely a reorientation of the lattice. The difference between twinning and slip should be carefully recognized since, in both cases, the lattice is sheared. Firstly, the deformation by means of slip occurs on individual lattice planes, as indicated in Figure 1.6 b. However, the shear associated with deformation twinning is uniformly distributed over a volume rather than localized on a discrete number of slip planes (Figure 1.6 a). Secondly, the shear associated with slip may be many times larger than the lattice space and depends on the number of dislocations emitted by the dislocation source. In contrast to slip, the shear due to twinning is small and the atoms on a single slip plane move only a fraction of an inter-atomic spacing relative to each other [16].

Although deformation twinning just accommodates a small amount of the total deformation strain, it is becoming increasingly important in explaining mechanical properties of metals because: (1) the lattice inside the twin may be realigned into a new orientation where the slip planes are more favorably aligned with respect to the applied stress. This means a relatively large deformation is permitted to occur inside the confined limits of twins

and (2) the intersections of twins are preferred positions for nucleation of new grains during annealing.

In Mg and other hcp metals, twinning plays a significant role during plastic deformation due to the limited number of slip systems for dislocation motion[17]. However the twinning and the associated dislocation processes in hcp metals are much more complex than those in FCC metals because hcp structure is a low-symmetry structure compared with FCC structure. The stacking sequence of close-packed plane  $\{0001\}$  in hcp metals is ABABAB... Since this structure has a plane of symmetry parallel to the close-packed plane, this plane cannot become a twin plane. This is also apparent from the letter sequence, which does not change on reversing. Actually the twin planes in hcp structure are pyramidal planes and the twin systems are  $\{10-12\}\langle 10-1-1\rangle$ ,  $\{10-11\}\langle 10-1-2\rangle$ ,  $\{11-22\}\frac{1}{3}\langle 11-2-3\rangle$  and  $\{11-21\}\frac{1}{3}\langle 1120\rangle$  [14, 18].

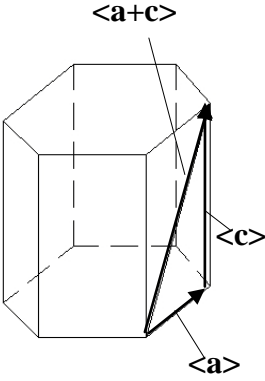
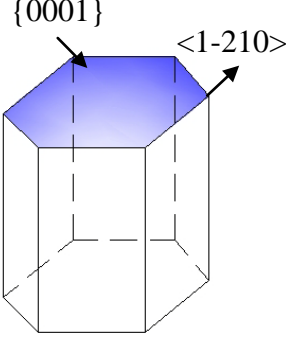
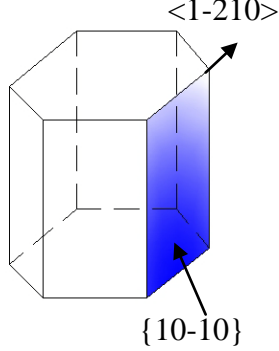
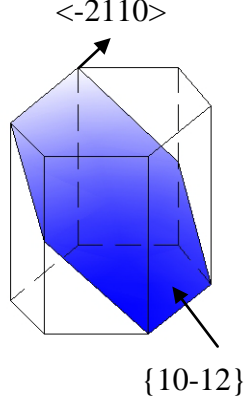
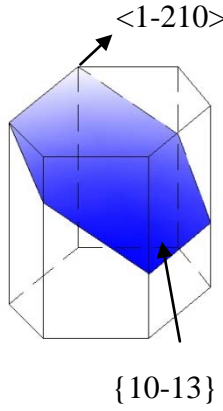
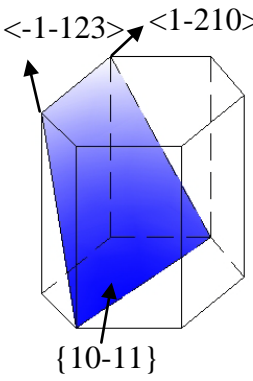
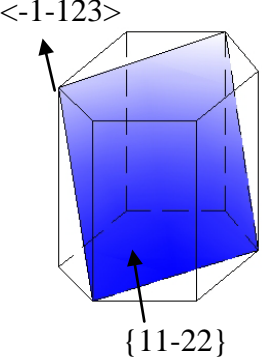
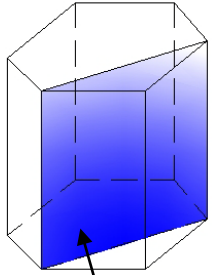
For Mg, there are two commonly observed twinning systems:  $\{10-12\}\langle 10-1-1\rangle$  and  $\{10-11\}\langle 10-1-2\rangle$  [18]. The first one,  $\{10-12\}\langle 10-1-1\rangle$ , is also called “extension twin” which is usually activated when tensile deformation is along the c-axis of hcp crystal [14] and the later one,  $\{10-11\}\langle 10-1-2\rangle$ , is a “contraction twin” which is a dominate twinning mode when the c-axis is under compression stress. These two twinning modes are of commercial interest. For instance, the thickness reduction during rolling of sheet involves the compression along c-axis and forging of extruded rod along the extrusion direction is a process of c-axis extension [19].

It is believed that the stress required for formation of deformation twinning is controlled mainly by the value of the stacking-fault energy (SFE) of the metal[20]. In order for the

metals to deform dominantly by twinning, the SFE should be less than a critical value [21, 22]. It was reported that the deformation twins occurred in Co-Ni alloys with a SFE in the range of 20 to 50 mJ/m<sup>2</sup>, while both the strain-induced martensitic transformation and deformation twinning occurred when the SFE was below 15 mJ/m<sup>2</sup> [21]. Zhu et al found deformation twinning in Mg-10% Ti (wt. %) processed by ball milling [20]. The activation of this deformation twins is mostly likely caused by the change of the general planer fault energy (GPFE) due to the Ti atoms segregating to the grain boundaries. It is reported that dislocation nucleation and emission from the grain boundaries became a major deformation mode in nanocrystalline (nc) FCC metals because of the lack of dislocation sources in the grain interior [23]. The dislocation nucleation and emission also likely play a major role in nc hcp metals [24]. The segregation of Ti atoms to the grain boundary region should strengthen the alloying effect to reduce GPFE energies on the dislocation nucleation and consequently promote the formation of deformation twins in the ball milled nc hcp Mg-Ti alloy [22].

Another important microstructural parameter influencing deformation twinning is the grain size of the metal [20]. For fcc metals, with decreasing grain size it becomes more difficult to deform by twinning in the coarse-grain size range [25], but twinning becomes easier once the grain size is smaller than 100 nm [19], although twinning may become difficult again when the grain size is too small (inverse grain size effect) [26]. In contrast, coarse-grained hcp metals usually need twinning to accommodate plastic deformation in addition to dislocation slip due to their lack of sufficient slip systems. However, twinning is rarely observed in nc hcp metals and alloys, with the exception of nc Zr processed by surface

**Table 1.3** The possible slip planes and associated dislocations in hcp metals.

$\langle a+c \rangle$ and $\langle a \rangle$ dislocations	$\langle a \rangle$ dislocation on basal plane	$\langle a \rangle$ dislocation on prismatic plane	$\langle a \rangle$ dislocation on pyramidal plane
$\langle a \rangle$ : $1/3\langle 11-20 \rangle$ $\langle a+c \rangle$ : $1/3\langle 11-23 \rangle$	$\{0001\} 1/3\langle 11-20 \rangle$	$\{10-10\} 1/3\langle 11-20 \rangle$	$\{10-12\} 1/3\langle 11-20 \rangle$
			
$\langle a \rangle$ dislocation on non-basal plane	$\langle a \rangle$ and $\langle a+c \rangle$ dislocation on pyramidal plane	$\langle a+c \rangle$ dislocation on pyramidal plane	No dislocation on this plane
$\{10-13\} 1/3\langle 11-20 \rangle$	$\{10-11\} 1/3\langle 11-20 \rangle$ $\{10-11\} 1/3\langle 11-23 \rangle$	$\{11-22\} 1/3\langle 11-23 \rangle$	$\{11-20\}$
			

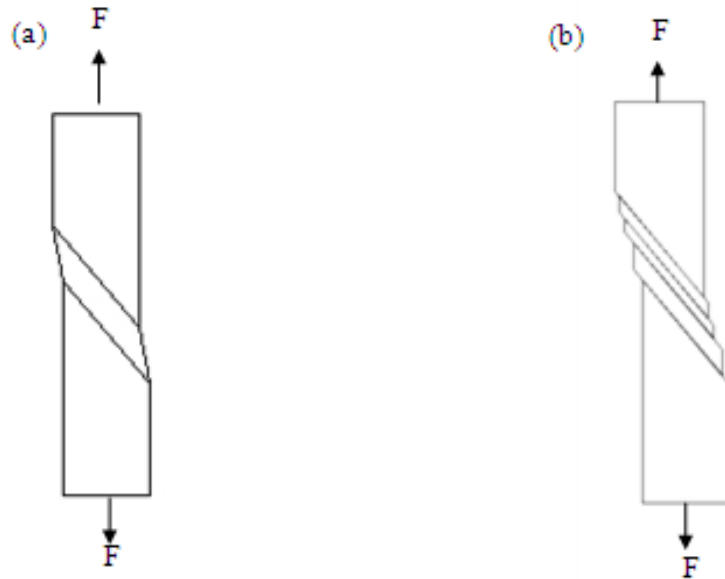


**Figure 1.6** Illustration of the shears associated with (a) twinning and (b) slip.

mechanical attrition (SMAT) [25] and nc Mg-Ti processed by ball milling [22]. As known, SMAT and ball milling processes involve the multidirectional impact on the materials resulting in the high strain rate severe plastic deformation. High strain rate deformation can promote the deformation twinning in nc hcp metals. This is because a higher strain rate deformation usually leads to a higher flow stress. Twins in Zr nucleate via successive emission of partial dislocations from grain boundaries or the overlapping of stacking faults and partial dislocations in grain interiors. As strain increases, twin nuclei grow up by adding more partial dislocations pairs into either side of the twin boundaries. The interaction between the formed twins and dislocations refines coarse grains into smaller ones, resulting in the nanocrystallization of zirconium.

Deformation twinning has been believed to significantly influence the mechanical properties of metals. Shen et al [19] reported that an electro-deposited Cu sample with a high density of nano-scale growth twins yielded an ultrahigh tensile strength of ~1 GPa and a considerable plastic strain larger than 13 %. Lu et al [27] synthesized high-purity Cu samples with nanoscale growth twins by using a pulsed electro-deposition technique. The tensile strength of the nano-twinned Cu was about 10 times higher than that of conventional coarse grained Cu, while retaining an electrical conductivity comparable to that of pure Cu. The ultrahigh strength originates from the effective blockage of dislocation motion by numerous coherent twin boundaries that possess an extremely low electrical resistivity, which is not the case for other types of grain boundaries.

### 1.3 Strengthening Strategies of Magnesium Alloys

In metals, plastic deformation occurs by means of dislocations movement and multiplication. In other words, it is the movement of dislocations in the material which allows for deformation. Thus, the principal of strengthening of metallic materials is to inhibit the dislocation movement. There are usually four strengthening strategies: solid solution hardening, precipitate hardening, strain hardening (work hardening) and grain boundary strengthening. The application of these strategies in strengthening of magnesium alloy will be introduced in the following sections.

#### 1.3.1 Solid Solution Strengthening

For the solid solution strengthening mechanism, solute atoms of alloying elements are dissolved or added into the matrix. Solid solution can result in either substitutional or interstitial point defects in the crystal, which depend on the size of the solute atom with

respect to that of the matrix atom. Substitutional solid solution strengthening occurs when the size of solute atom is large enough that solute atom can replace solvent atoms in their lattice positions. An interstitial solid solution will form if the size of solute atom is much smaller than that of the solvent atom. Once solid solutions are formed, the lattice of the matrix is distorted by the substitutional or interstitial solute atoms and local stress fields are formed that interact with those of the dislocations, impede dislocations motion and causing an increase in the macroscopic yield stress of the material.

It was found in a Mg-Al alloy that the 0.2% proof strength increased linearly with  $c^n$ , where  $c$  is the solution atom concentration and  $n=1/2\sim 2/3$  [28]. By adding RE elements, such as Gd, Y and Zr, solution hardening is more beneficial in improving strength of magnesium alloys than Al and Zn element due to the large misfit between RE atomic size and Mg atomic size [29, 30].

### 1.3.2 Precipitate Hardening

Precipitate hardening has been extensively used to increase the strength in a wide range of metallic materials. The principle of precipitate strengthening is to produce a particular dispersion of second phase particles serving as obstacles to dislocation motion. The degree of precipitates strengthening is mainly dependent upon the metallic systems involved, the volume fraction, the size of the particle, and the nature of the interaction of the particles with dislocations [30]. The precipitation hardening process is a thermodynamic and kinetic process which involves sufficient dissolution of the second phase in the matrix at elevated temperatures and then aging at a relatively lower temperature to considerably reduce the solubility of the second phase such that precipitation forms in the matrix. The equilibrium

phase diagram of alloy system is particularly useful in determining the solution and aging temperature, the extent of dissolution and precipitation, and the volume fraction of fine precipitated particles that contribute to precipitation hardening [30].

In the early stages of precipitation, the interaction between the strain fields of the coherent particles and the dislocations provides a greater strengthening effect than that would be expected from the precipitates/zones/ clusters alone. This mechanism is called ‘coherency strengthening’. Mott and Nabarro described that a dislocation was bent to lie in low energy positions with respect to the strain fields and consequently, any force applied must overcome an enhanced number of obstacles without the assistance of segments of dislocation in high energy positions before stressing [31]. For Mg alloys, it was reported that the addition of rare earth elements (RE) can improve their mechanical properties at room and elevated temperatures due to solution hardening and precipitate hardening. However the solubility of RE in magnesium is smaller than other well known solution-hardening elements, such as aluminum and zinc. Therefore, the most promising strengthening mechanism of Mg alloys is precipitate hardening [32]. Since Mg-Gd-Y-Ag-Zr is the targeted Mg alloys in this thesis, here we focus our discussion on the precipitates in this serial of Mg alloy.

In Mg-Gd-Y-Zr alloy system, the precipitate sequence is  $\alpha'$ (cph)  $\rightarrow \beta''$ (D0<sub>19</sub>)  $\rightarrow \beta'$ (cbco)  $\rightarrow \beta_1$ (fcc)  $\rightarrow \beta$ (fcc) [33]. In the very early stage of ageing, very fine spheroidal  $\beta''$  precipitates formed. They are mainly responsible for the small increase in the age hardness during that ageing stage ( $\sim 0.5$  h). The D0<sub>19</sub> metastable phase,  $\beta''$ , is hexagonal with  $a=2a_{Mg}=0.64$  nm,  $c=c_{Mg}=0.52$  nm and is coherent with the  $\alpha$ -Mg matrix [34]. Continuous ageing will lead to

the formation of  $\beta$  precipitates. The size and volume fraction of the  $\beta'$  precipitates increase with the prolonging of ageing time and this may be attributed to the gradual increase in the age hardness before peak ageing is reached. In the peak-ageing condition, the microstructure contained predominantly  $\beta'$  precipitates. The c-base centered orthorhombic (cbco) metastable  $\beta'$  phase has the lattice parameter of  $a=2a_{Mg}=0.64$  nm,  $b=8d_{(10-10)Mg}=2.22$  nm and  $c=c_{Mg}=0.52$  nm [33]. In the process of overaging, the  $\beta'$  phase coarsens and the  $\beta_1$  phase precipitates. Long-term ageing leads to the formation of coarse equilibrium  $\beta$  phase which is predominant in the microstructure, and this is the cause of the significant decrease in the ageing hardness. It was found that the addition of Zn and/or Ag can lead to a substantial enhancement of the age-hardening response of the Mg–Gd–Y–Zr alloy [35]. The maximum hardness values achievable during isothermal aging at 200 and 250 °C are obtained in the Mg–Gd–Zn alloy that contains both Ag and Zn additions, i.e. Mg–6Gd–2Ag–1Zn–0.6Zr alloy. This remarkable improvement in precipitation-hardening is associated with the formation of a dense and uniform distribution of nano-scale basal precipitate plates within the matrix phase.

### 1.3.3 Strain Hardening

Strain hardening, also known as work hardening, is the strengthening of a metal by plastic deformation at a temperature usually below recrystallization temperature. The density of defects, such as dislocation and/or twinning, will be increased in the crystal during plastic deformation. Because the repulsive or attractive interaction between the stress fields of dislocations is intensified and the motion of dislocation is impeded, increasing the dislocation density increases the yield strength of processed materials. This process is easily observed during plastic deformation of a material, such as rolling, extrusion, drawing and forging.

However most Mg alloys cannot be cold worked due to their poor formability at room temperature. Plastic deformation of Mg alloys is usually conducted at an elevated temperature, during which dislocations may annihilate or recover. Actually, the competition between dislocation accumulation and annihilation is usually accompanied by dynamic recrystallization (DRX) [36-38]. DRX grains are usually defects-free, which may eliminate the strengthening effect of work hardening. However, DRX can lead a significant grain refinement and strengthen the materials with excess grain boundaries.

#### 1.3.4 Grain Boundary Strengthening

Grain-boundary strengthening is a method of strengthening materials by changing their average crystallite (grain) size. In a polycrystalline metal, the grain size has a tremendous influence on the mechanical properties. Since the lattice orientation of adjacent grains are different, it requires more energy for a dislocation to change directions and move into the adjacent grain. The grain boundary is also much more disordered than the interior of the grain, which also prevents the dislocations from moving on a continuous slip plane [39]. Impeding the dislocation movement will hinder the onset of plasticity and hence increase the yield strength of the material. The relation between yield stress and grain size is described mathematically by the Hall-Petch equation. In Mg alloys, grain refinement is a significantly important procedure that improves mechanical properties [32-34]. Actually, the above four strengthening mechanisms are barely applied individually in pre-treatment and plastic deformation of Mg alloys. Choosing the appropriate combination of these strengthening strategies can greatly improve the mechanical properties.

## REFERENCES

- [1] McCormick SHaPG. The synthesis and properties of nanocrystalline magnesium by ball milling. Synthesis of lightweight metals III: TMS Warrendale, PA; 1999.
- [2] M. Pekguleryuz PL, D. Argo. Magnesium die casting alloy AJ62x with superior creep resistance, ductility and die castability. In: Ruden T, editor. Lightweight Magnesium Technology 2001-2005. Warrendale, PA: SAE International; 2006.
- [3] Mordike BL, Ebert T. Magnesium - properties - applications - potential. Materials Science and Engineering: A 2001;302:37-45.
- [4] Hull D, Bacon DJ. Introduction to dislocations. 4th ed. Oxford, UK: Elsevier Ltd.; 2001.
- [5] Dillamore IL, Hull D - Introduction to dislocations. J I Met 1966;94:95.
- [6] Yoo MH. Slip, Twinning, and fracture in hexagonal close-packed metals. Metall Trans A 1981;12:409-18.
- [7] Taylor GI. Plastic strain in metals. J I Met 1938;62:307-24.
- [8] Groves GW, Kelly A. Independent slip systems in crystals. Philos Mag 1963;8:877-87.
- [9] Wonsiewi.Bc, Backofen WA. Plasticity of magnesium crystals. Trans. TMS- AIME 1967;239:1422-31.
- [10] Flynn PW, Mote J, Dorn JE. On the Thermally activated mechanism of prismatic slip in magnesium single crystals. T Metall Soc Aime 1961;221:1148-54.
- [11] Reedhill RE, Robertson WD. Deformation of magnesium single crystals by nonbasal slip. Transactions of the American Institute of Mining and Metallurgical Engineers 1957;209:496-502.

- [12] Reedhill RE, Robertson WD. Pyramidal slip in magnesium. Transactions of the American Institute of Mining and Metallurgical Engineers 1958;212:256-9.
- [13] Agnew SR, Duygulu O. Plastic anisotropy and the pole of non-basal slip in magnesium alloy AZ31B. Int J Plasticity 2005;21:1161-93.
- [14] Barnett MR. Twinning and the ductility of magnesium alloys: part II. “contraction” twins. Materials Science and Engineering: A 2007;464:8-16.
- [15] Obara T, Yoshinga H, Morozumi S.  $\{1122\}$   $\langle 1123 \rangle$  slip system in magnesium. Acta Metall Mater 1973;21:845-53.
- [16] Li B, Ma E. Zonal dislocations mediating twinning in magnesium. Acta Materialia 2009;57:1734-43.
- [17] Yoo M. Slip, Twinning and fracture in hexagonal close-packed metals. Metallurgical and Materials Transactions A 1981;12:409-18.
- [18] Christian JW, Mahajan S. Deformation twinning. Prog Mater Sci 1995;39:1-157.
- [19] El-Danaf E, Kalidindi S, Doherty R. Influence of grain size and stacking-fault energy on deformation twinning in fcc metals. Metallurgical and Materials Transactions A 1999;30:1223-33.
- [20] Remy L, Pineau A. Twinning and strain-induced F.C.C.  $\rightarrow$  H.C.P. transformation in the Fe-Mn-Cr-C system. Mater Sci Eng 1977;28:99-107.
- [21] Oh BW, Cho SJ, Kim YG, Kim YP, Kim WS, Hong SH. Effect of aluminium on deformation mode and mechanical properties of austenitic Fe-Mn-Cr-Al-C alloys. Materials Science and Engineering: A 1995;197:147-56.

- [22] Wu XL, Youssef KM, Koch CC, Mathaudhu SN, Kecskés LJ, Zhu YT. Deformation twinning in a nanocrystalline hcp Mg alloy. *Scripta Materialia* 2011;64:213-6.
- [23] Wu XL, Zhu YT. Inverse grain-size effect on twinning in nanocrystalline Ni. *Phys Rev Lett* 2008;101:025503.
- [24] Meyers MA, Vöhringer O, Lubarda VA. The onset of twinning in metals: a constitutive description. *Acta Materialia* 2001;49:4025-39.
- [25] Zhang L, Han Y. Twins formation and their role in nanostructuring of zirconium. *Materials Science and Engineering: A* 2009;523:130-3.
- [26] Shen YF, Lu L, Lu QH, Jin ZH, Lu K. Tensile properties of copper with nano-scale twins. *Scripta Materialia* 2005;52:989-94.
- [27] Lu L, Shen Y, Chen X, Qian L, Lu K. Ultrahigh strength and high electrical conductivity in copper. *Science* 2004;304:422-6.
- [28] Wang J, Meng J, Zhang D, Tang D. Effect of Y for enhanced age hardening response and mechanical properties of Mg–Gd–Y–Zr alloys. *Materials Science and Engineering: A* 2007;456:78-84.
- [29] Wang Q, Chen J, Zhao Z, He S. Microstructure and super high strength of cast Mg-8.5Gd-2.3Y-1.8Ag-0.4Zr alloy. *Materials Science and Engineering: A* 2010;528:323-8.
- [30] Gladman T. Precipitation hardening in metals. *Mater Sci Tech-Lond* 1999;15:30-6.
- [31] Kelly A, Nicholson RB. Precipitation hardening. *Prog Mater Sci* 1963;10:151-391.
- [32] He SM, Zeng XQ, Peng LM, Gao X, Nie JF, Ding WJ. Microstructure and strengthening mechanism of high strength Mg–10Gd–2Y–0.5Zr alloy. *J Alloy Compd* 2007;427:316-23.

- [33] He SM, Zeng XQ, Peng LM, Gao X, Nie JF, Ding WJ. Precipitation in a Mg–10Gd–3Y–0.4Zr (wt.%) alloy during isothermal ageing at 250°C. *J Alloy Compd* 2006;421:309-13.
- [34] Smola B, Stulíková I, von Buch F, Mordike BL. Structural aspects of high performance Mg alloys design. *Materials Science and Engineering: A* 2002;324:113-7.
- [35] Gao X, Nie JF. Enhanced precipitation-hardening in Mg–Gd alloys containing Ag and Zn. *Scripta Materialia* 2008;58:619-22.
- [36] Pérez-Prado MT, del Valle JA, Contreras JM, Ruano OA. Microstructural evolution during large strain hot rolling of an AM60 Mg alloy. *Scripta Materialia* 2004;50:661-5.
- [37] Chen Y, Wang Q, Peng J, Zhai C, Ding W. Effects of extrusion ratio on the microstructure and mechanical properties of AZ31 Mg alloy. *J Mater Process Tech* 2007;182:281-5.
- [38] Guo Q, Yan HG, Chen ZH, Zhang H. Grain refinement in as-cast AZ80 Mg alloy under large strain deformation. *Mater Charact* 2007;58:162-7.
- [39] Callister WC JR. *Materials Science and Engineering: An Introduction*. 7 th ed. New York, NY: John Wiley&Sons, Inc. ; 2007, p.189.

## CHAPTER 2: Experiments

The casting procedures of the Mg-8.5Gd-2.3Y-1.8Ag-0.4Zr (wt.%) ingot investigated in this work can be found in reference [1]. Specimens were solution treated (T4 treatment) in a vacuum furnace at 500 °C for 12 hours and then quenched into room temperature silicon oil. The details about solution treatment can be found in Appendix A. T4 treated specimens were then hot rolled at 450 °C with thickness reduction of 50 %, 60%, 70% 78% and 88%. Specimens were heated in a furnace with protective gas at 450°C for 15 minutes between each pass and then rolled immediately with a thickness reduction of < 5% per pass. The rolling mill setup is shown in Fig. 2.1. Room temperature tensile test samples were cut from the rolling plane and pulled to failure in the direction parallel to rolling direction using strain rate of  $2.35 \times 10^{-3} \cdot s^{-1}$ . The gauge length, width and thickness of the testing samples were 7 mm, 1 mm and 0.3 mm, respectively.

Microstructures of T4 treated and rolled samples were characterized using optical microscopy (OM) and transmission electron microscopy (TEM). OM specimens were ground, polished and, etched in a mixed acid of 3 g picric acid, 50 ml ethanol, 20 ml acetic acid and 20 ml water. TEM specimens were polished using 0.3  $\mu\text{m}$  silicon carbide lapping film to a thickness of  $\sim 20 \mu\text{m}$  and then ion milled to perforation. Ion milling was performed at -100 °C with low angle ( $< 4^\circ$ ) and low energy ( $< 2.0 \text{ keV}$ ). Immediately after sample preparation, TEM observation was conducted on JEM-2000FX and JEM-2010 F operating at 200 kV. Scanning electron microscopy (SEM) with EDS was used to quantify the contents of the alloying elements in matrix of the rolled samples. X-ray diffraction was used to characterize the texture of the rolled samples.

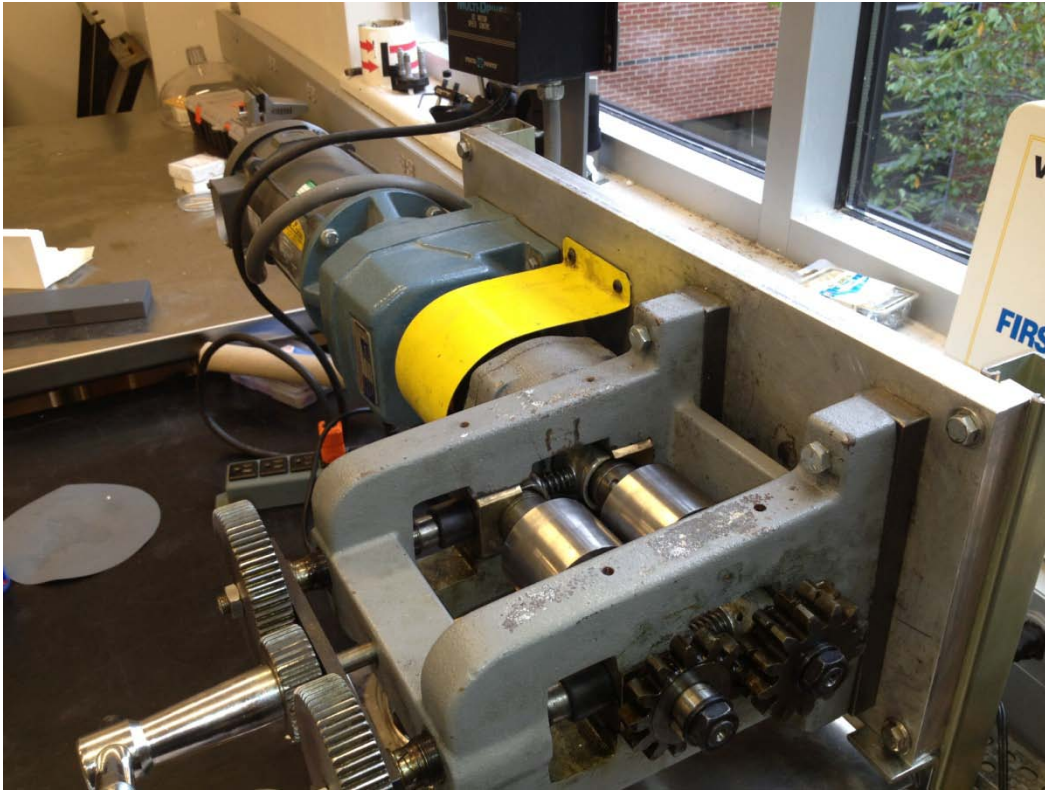


**Figure 2.1** Rolling machine used in current experiment.

## REFERENCES

- [1] Wang Q, Chen J, Zhao Z, He S. Microstructure and super high strength of cast Mg-8.5Gd-2.3Y-1.8Ag-0.4Zr alloy. *Materials Science and Engineering: A* 2010;528:323-8.

## CHAPTER 3: Ultrastrong Mg-Alloy via Nano-Spaced Stacking Faults

### 3.1 Introduction

Magnesium and its alloys have attracted extensive attention in recent years due to their abundance, low-density, good castability and recyclability [1-4]. However, the application of Mg alloy has been substantially hindered by their relatively low strengths (tensile yield strength: ~100MPa to 250 MPa for commercial casting Mg alloys [5, 6]) and limited ductility (elongation: 2% to 8% [5-7]) at room temperature. Outside of traditional precipitation control, Mg-alloy strengthening typically relies on two general approaches: non-traditional, esoteric processing and grain refinement. An example of non-traditional processing for high strength is rapid solidification/powder metallurgy (RS/PM), which has been used to obtain a yield strength of ~600 MPa in a Mg-Zn-Y alloy with uniform distribution of long-period ordered structures [8]. While the resultant properties are remarkable, such unconventional processing technologies limit potential industrial application. In addition, the ultrahigh strength is usually accompanied by marked losses in the ductility [8].

The second general approach of grain refinement for strengthening has been used to obtain ultrafine ( $< 1 \mu\text{m}$ ) grains in Mg-alloys [9-12]. The high concentration of grain boundaries (GBs) in the ultrafine-grained microstructure provides barriers to motion of dislocations and consequently promotes the strength improvement. Nevertheless GB strengthening mechanisms alone provided limited contribution to macroscopic yield strengths, which, in these reports [9-12], are typically less than 400 MPa. More importantly, refining the grain size is reported to suppress the propensity of deformation twinning which, in addition to dislocation slip, is an important mechanism for enhancing strength and ductility

[13-18]. Ultrafine-grained microstructures also suffer from strength reduction via grain growth at a relatively low temperature ( $0.32 T_m$ ) [19] thus limiting the potential for further shaping or processing.

In this paper, we report a new mechanism for inducing ultrahigh strengths (yield strength:  $\sim 575$  MPa, ultimate strength:  $\sim 600$  MPa) and maintaining moderate ductility (uniform elongation:  $\sim 3\%$  to  $4\%$ ) via conventional processing (hot-rolling) of a Mg-alloy (Mg-8.5Gd-2.3Y-1.8Ag-0.4Zr (wt.%)) with relatively large grain sizes ( $13 \mu\text{m}$ ). We propose that the introduction of a high density of stacking faults with nanoscale spacing provides for dislocation pile-up strengthening and retention of work hardening for enhanced ductility.

### 3.2 Experimental Procedures

The casting method used to produce the Mg-8.5Gd-2.3Y-1.8Ag-0.4Zr (wt.%) (hereafter referred to as “Mg-alloy”) ingot can be found in reference [20]. The Mg-alloy was then T4 treated ( $500^\circ\text{C}$  for 12 hours in a vacuum furnace and quenched in room temperature silicon oil); the T4 conditions serve as a baseline for property assessment. Prior to each rolling pass, specimens were heated in a furnace at  $450^\circ\text{C}$  for 15 minutes and rolled on a conventional hot roller with a thickness reduction of  $< 5\%$  per pass to a total rolling reduction of  $50\%$ - $88\%$ . Rolled specimens were air-cooled to room temperature. Tensile test samples were cut on the rolling plane and pulled to failure in the direction parallel to the rolling direction using a strain rate of  $2.35 \times 10^{-3} \cdot \text{s}^{-1}$ . The gauge length and width of the testing samples are 7 mm and 1 mm, respectively. The surfaces of the gauge region were polished to mirror-like surfaces before tensile testing and at least three samples for each rolling parameter were tested. For TEM studies, specimens were gently polished and then ion milled to perforation on a cold

stage with a low angle and a low energy ion beam. Microscopy was conducted on a JEM-2000FX and a JEM-2010 F operating at 200 kV.

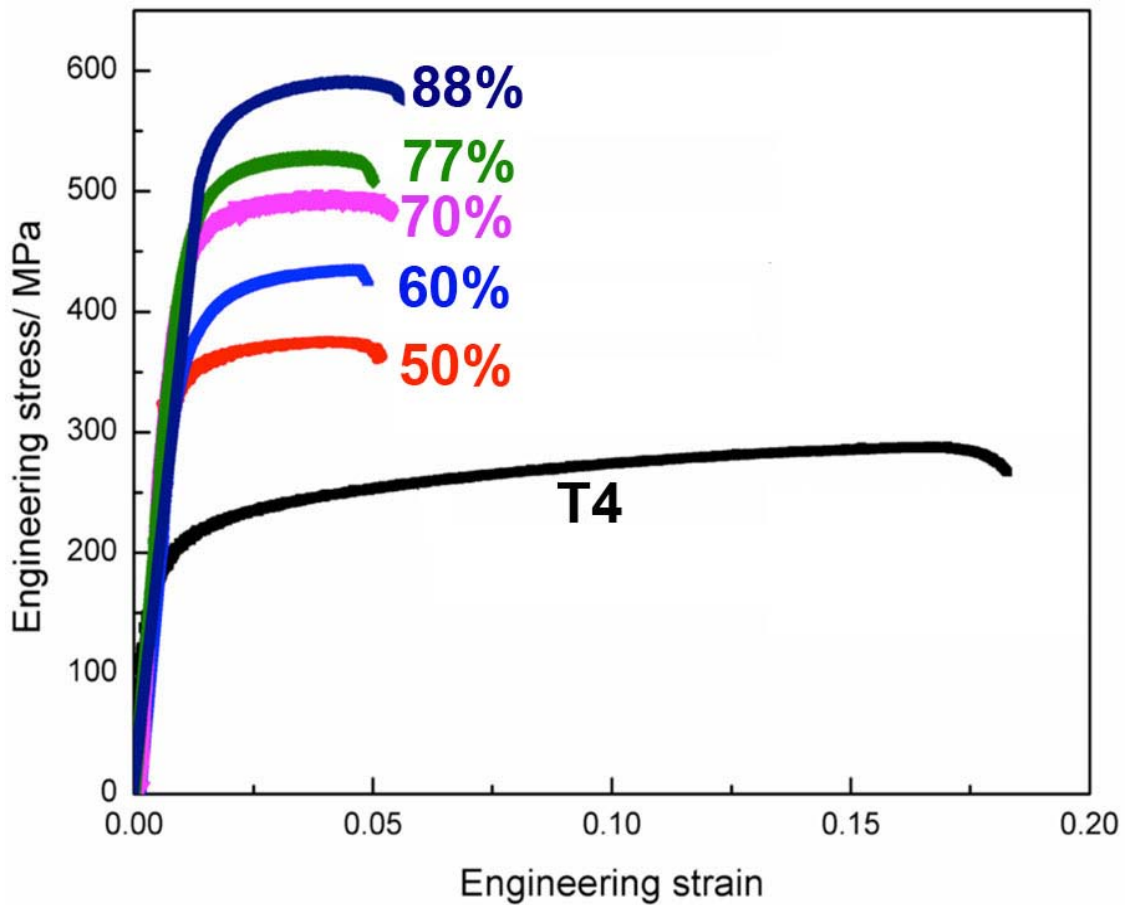
### 3.3 Results and Discussion

Figure 3.1 shows the tensile engineering stress-strain curves of the Mg alloy samples after T4 treatment, and after hot rolling to different thickness reductions. Both the tensile yield strength and ultimate strength of the rolled samples increase as the rolling strain increases and the maximum values reach 575 MPa and ~600 MPa, respectively, which are more than two times of the values of the T4 treated baseline. Compared with the yield strength and uniform elongation values in various similar Mg alloys [9, 11, 21-54] as shown in Fig. 3.2, the current results show an extraordinary combination of ultrahigh strength and reasonably good ductility. Most importantly, the elongation to failure of the processed Mg-alloy retains a moderate level (5% to 6%) without diminishing during the hot rolling process. It should be mentioned that there was only one other reference [8] reported that the yield strength of a Mg-Zn-Y alloy can reach 600 MPa, which was produced by rapid solidification/powder metallurgy (RS/PM) plus extrusion. Since this article was published on 2001 [8], we are the first group which can produce an ultrastrong Mg alloy with yield strength close to 600 MPa.

TEM analysis was performed to probe the main microstructural features that are responsible for the observed strengthening in the hot rolled Mg-8.5Gd-2.3Y-1.8Ag-0.4Zr (wt.%) alloy. It was observed that beyond 50% thickness reductions, basal plane stacking faults (SFs) become the primary crystalline defects (see Fig. 3.3). The (0001) basal plane SFs

are further verified by the presence of streakings along the [0001] direction in the selected area diffraction pattern [55] (Fig. 3.3d).

The average spacing between adjacent SFs,  $d$ , decreases as rolling reduction increases. At 88% thickness reduction, nano-spaced SFs with an average spacing  $d \sim 16$  nm were formed in most coarse grains. The formation of high density of SFs is due to the low stacking fault energy (SFE) of this Mg alloy. It has been reported that both Gd and Y lower the SFE



**Figure 3.1** Engineering stress-strain curves of Mg-8.5Gd-2.3Y-1.8Ag-0.4Zr (wt.%) samples under T4 treatment and hot rolling with different thickness reductions (marked by the curves).

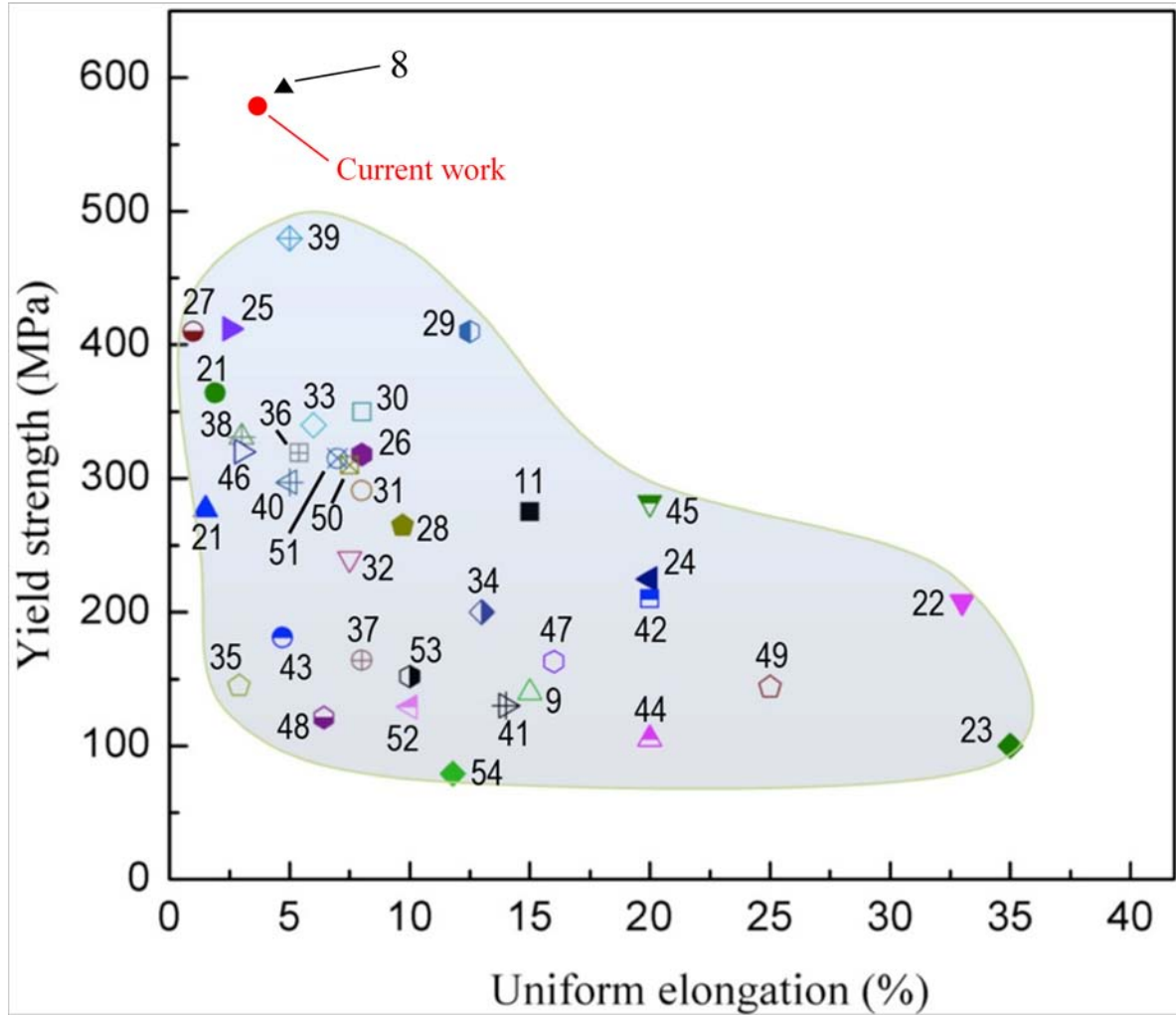


**Figure 3.2** Summary of room temperature tensile yield strength and uniform elongation of previous reports and our current work. The criteria used to summarize and reproduce this figure are (1) only room temperature uniaxial tensile test results were included, (2) the gauge length of tensile test sample was larger than 5 mm, and (3) the stress-strain curve must be indicated in the individual report in order to reproduce the uniform elongation. The reference number is by the data point.

of Mg [56, 57]. The stacking faults can be formed by the dissociation of a full dislocation into two partial dislocations on the basal plane during plastic deformation. The partial dislocations can be driven apart by applied stress to form a wide planar stacking fault ribbon [58].

Plotting the yield strength against the reciprocal of average spacing of SFs,  $1/d$ , reveals a linear relationship (Fig. 3.4), i.e.

$$\sigma_{0.2} = \sigma_0 + \frac{k}{d} \quad (3.1)$$

where  $d$  is the mean spacing between adjacent SFs,  $\sigma_0$  is the total strength contributed by strengthening mechanisms other than SFs. In the current Mg alloy, a number of typical strengthening mechanisms are expected to be active, such as solid-solution strengthening, grain refinement, dynamic precipitation and textural strengthening.

The linear relationship between the strength and reciprocal of the SF spacing indicates that the SFs are very effective in improving the strength. Fitting the data in Fig. 3.4 with Eq. 1 yields  $\sigma_0 = 340$  MPa, and  $k = 3780$  MPa•nm. In other words, introducing SFs with an average spacing of 16 nm increased the yield strength of the Mg alloy by 70% from 340 MPa to 575 MPa. This indicates that SFs are very effective in improving the strength of Mg alloys. The fact that SFs increased the strength, but did not decrease the ductility (See Fig. 3.1) makes SFs even more attractive for improving mechanical properties of Mg alloys. This discovery is especially important for hcp metals and alloys, because twinning, an effective approach for improving strength and ductility for fcc metals and alloys, becomes very difficult to activate in hcp metals when the grain sizes are below a few hundred nanometers

[13, 14], making it very difficult to combine the strengthening effects of refining grains and introducing twins.

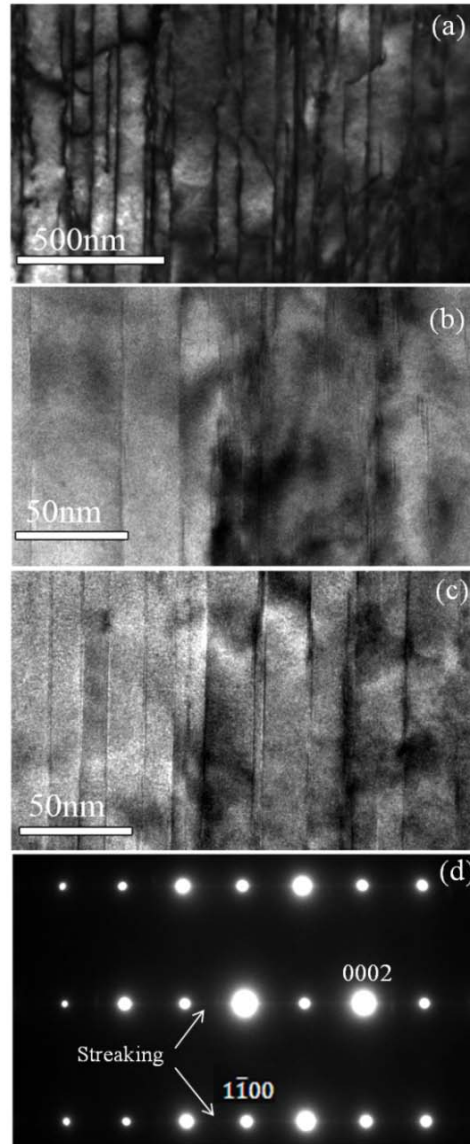


**Figure 3.3** TEM images of Mg-8.5Gd-2.3Y-1.8Ag-0.4Zr (wt.%) alloy samples with various rolling thickness reductions: (a) 50%,  $d=55$  nm, (b) 70%,  $d=25$  nm and (c) 88%,  $d=16$  nm. Image (d) is the SAD pattern of the 70% rolled sample in which the streaking verifies the basal plane SFs.

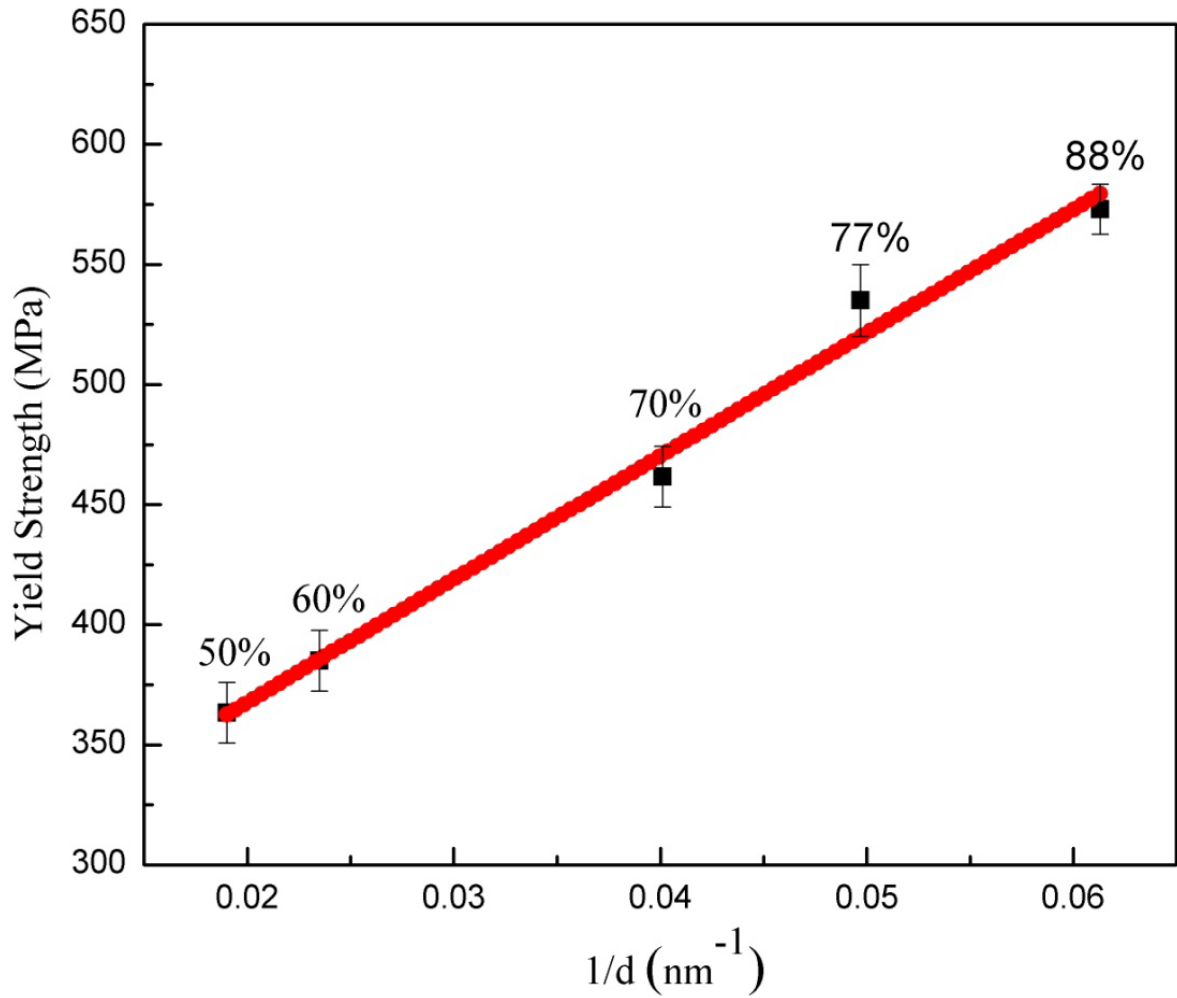


**Figure 3.4** Yield strength vs the reciprocal of mean spacing between SFs of rolled samples with different thickness reduction. The number by each data point indicates the thickness reduction by hot rolling.

SFs on basal planes are expected to provide the similar effect of impeding dislocation movement as reported for nano-twinned electrodeposited Cu [17]. As dislocations slip and encounter with SF boundaries, they can either cut or interact with SFs in order to move and

facilitate plastic deformation or accumulate around SF boundaries and accommodate increased strain hardening [59].

In order to probe the dislocation interactions with SFs, post-mortem TEM observation (Fig. 3.5) was conducted on tension-tested samples that were initially hot rolled for 88% to produce nano-spaced SFs. Figure 3.5a shows a distinctly different feature of fragmented SFs as compared to Fig. 3c. Some SFs have been broken into short segments (Fig. 3.5a), and a high density of dislocations is trapped between SFs (Fig. 3.5b). As shown in Fig. 3.5a, some SF segments are well aligned along a line, suggesting that they were most likely formed from a single SF that was cut by dislocations slipping on pyramidal or prism planes.

Since the hot rolling produced a strong texture with the basal planes parallel to the rolling direction, the tensile stress direction is nearly parallel to the basal plane during tensile testing. This makes it necessary to activate  $\langle c \rangle$  and/or  $\langle c+a \rangle$  dislocations to slip on the pyramidal or prisms slip planes. Such dislocation slip will encounter SFs, which will either cut SFs into segments or be blocked by the SFs if the applied stress is not high enough to cut the SFs. These dislocation-SF interactions are similar to the dislocation-twin interactions in an fcc system [59]. More investigations are needed to study the interaction details.

The blocking of dislocations by SFs and the cutting of SFs by dislocations will hinder the slip of dislocations, which consequently increases the yield strength. The high density of dislocations between SFs after tensile testing indicates that SFs are effective in blocking and accumulating dislocations, which will enhance strain-hardening rate and consequently help with ductility retention. This explains why no ductility reduction is observed with increasing strength when a high density of SFs is introduced into the Mg alloy.

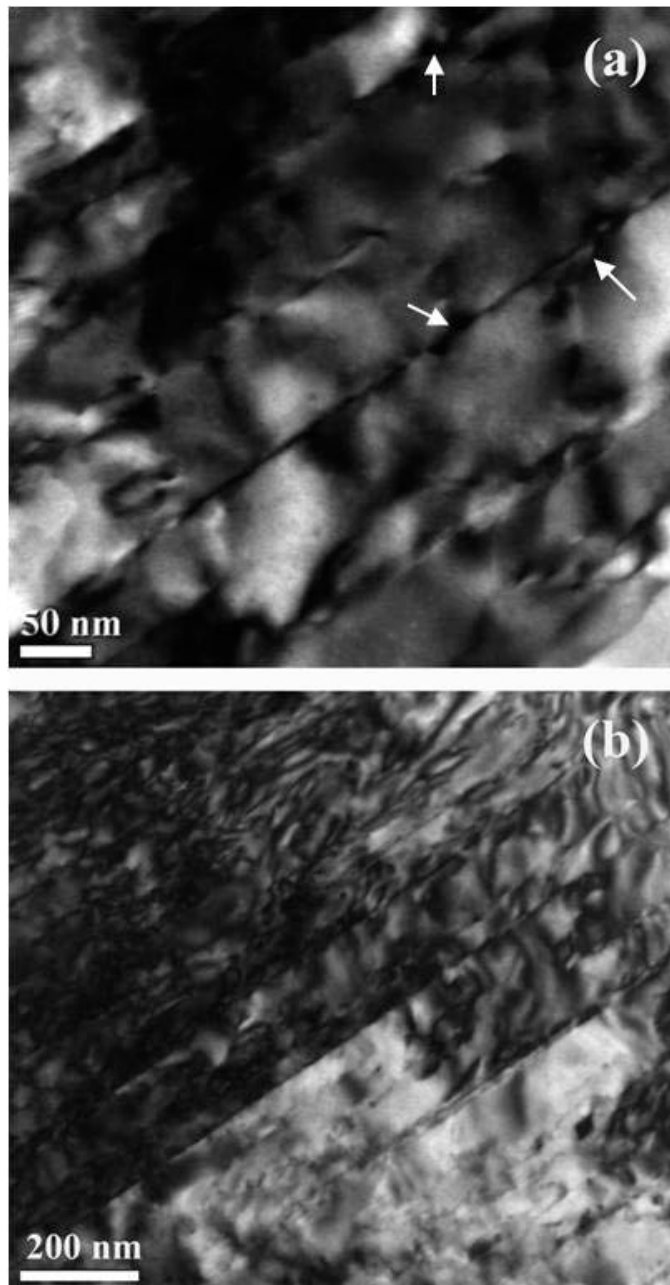


**Figure 3.5** TEM images of 88% hot rolled sample after tensile test. (a) Fragments of SFs cut by the dislocations. (b) The yellow dash line indicates SFs and white circles mark the fragmented SFs with few atomic layer spacing steps.

### 3.4 Summary

Conventional hot rolling was conducted on a T4 treated Mg-8.5Gd-2.3Y-1.8Ag-0.4Zr (wt.%) alloy with thickness reduction up to 88%. Unprecedented strength and moderate ductility (YS ~575 MPa, UTS ~ 600 MPa, uniform elongation ~5.2%) was observed. TEM studies show that a high density of nano-spaced SFs are the main defects inside of grain and their density increased as rolling thickness reduction increased. Strength of processed Mg alloy was found to increase as the mean spacing between adjacent (SFs) decreased. Nano-spaced SFs are found to be tremendously effective in impeding the movement of dislocations and retaining strain hardening. Activation of non basal dislocations during tensile testing accounts for the detected moderate ductility, in addition to the capability of retaining strain hardening. It is expected that optimization of approaches that introduce a high density of nano-spaced SFs will enable other Mg-alloys with concurrent high strength and good ductility.

## REFERENCES

- [1] Nie JF, Gao X, Zhu SM. Enhanced age hardening response and creep resistance of Mg-Gd alloys containing Zn. *Scripta Mater* 2005;53:1049-53.
- [2] He SM, Zeng XQ, Peng LM, Gao X, Nie JF, Ding WJ. Microstructure and strengthening mechanism of high strength Mg-10Gd-2Y-0.5Zr alloy. *J Alloys Compd* 2007;427:316-23.
- [3] Honma T, Ohkubo T, Kamado S, Hono K. Effect of Zn additions on the age-hardening of Mg-2.0Gd-1.2Y-0.2Zr alloys. *Acta Mater* 2007;55:4137-50.
- [4] Yamada K, Hoshikawa H, Maki S, Ozaki T, Kuroki Y, Kamado S, et al. Enhanced age-hardening and formation of plate precipitates in Mg-Gd-Ag alloys. *Scripta Mater* 2009;61:636-9.
- [5] Mordike BL, Ebert T. Magnesium - properties - applications - potential. *Mater Sci Eng A* 2001;302:37-45.
- [6] Pekguleryuz M, Labelle D, Argo D. Magnesium die casting alloy AJ62x with superior creep resistance. In: Liu ZK, Ruden T, editors. *Lightweight Magnesium Technology 2001-2005*: SAE International, Warrendale, PA, ; 2006. p. 269.
- [7] Champrenault M, Maas CA, Cunningham J. Magnesium powertrain mount brackets: new application of material being used in this sub-system for vehicle mass reduction. In: Liu ZK, Powell BR, Zheng WY, editors. *Magnesium Technologies 2007*: SAE International, Warrendale, PA, ; 2007. p. 57.
- [8] Inoue A, Kawamura Y, Matsushita M, Hayashi K, Koike J. Novel hexagonal structure and ultrahigh strength of magnesium solid solution in the Mg-Zn-Y system. *J Mater Res* 2001;16:1894-900.

- [9] Yamashita A, Horita Z, Langdon TG. Improving the mechanical properties of magnesium and a magnesium alloy through severe plastic deformation. *Mater Sci Eng A* 2001;300:142-7.
- [10] Ma AB, Jiang JH, Saito N, Shigematsu I, Yuan YC, Yang DH, et al. Improving both strength and ductility of a Mg alloy through a large number of ECAP passes. *Mater Sci Eng A* 2009;513-14:122-7.
- [11] Yoshida Y, Arai K, Itoh S, Kamado S, Kojima Y. Realization of high strength and high ductility for AZ61 magnesium alloy by severe warm working. *Sci Tech Adv Mater* 2005;6:185-94.
- [12] Yoshida Y, Cisar L, Kamado S, Kojima Y. Effect of microstructural factors on tensile properties of an ECAE-processed AZ31 magnesium alloy. *Mater Trans* 2003;44:468-75.
- [13] Wu XL, Youssef KM, Koch CC, Mathaudhu SN, Kecskes LJ, Zhu YT. Deformation twinning in a nanocrystalline hcp Mg alloy. *Scripta mat* 2011;64:213-6.
- [14] Zhu YT, Liao XZ, Wu XL. Deformation twinning in nanocrystalline materials. *Prog Mater Sci* 2012;57:1-62.
- [15] Zhao YH, Bingert JE, Liao XZ, Cui BZ, Han K, Sergueeva AV, et al. Simultaneously increasing the ductility and strength of ultra-fine-grained pure copper. *Adv Mater* 2006;18:2949-53.
- [16] Zhao YH, Zhu YT, Liao XZ, Horita Z, Langdon TG. Tailoring stacking fault energy for high ductility and high strength in ultrafine grained Cu and its alloy. *Appl Phys Lett* 2006;89:121906.
- [17] Lu K, Lu L, Suresh S. Strengthening materials by engineering coherent internal boundaries at the nanoscale. *Science* 2009;324:349-52.

- [18] Lu L, Shen YF, Chen XH, Qian LH, Lu K. Ultrahigh strength and high electrical conductivity in copper. *Science* 2004;304:422-6.
- [19] Lian JS, Valiev RZ, Baudelet B. On the enhanced grain-growth in ultrafine grained metals. *Acta Metall Mater* 1995;43:4165-70.
- [20] Wang QD, Chen J, Zhao Z, He SM. Microstructure and super high strength of cast Mg-8.5Gd-2.3Y-1.8Ag-0.4Zr alloy. *Mater Sci Eng A* 2010;528:323-8.
- [21] Chino Y, Mabuchi M. Influences of grain size on mechanical properties of extruded AZ91 mg alloy after different extrusion processes. *Advanced Engineering Materials* 2001;3:981-3.
- [22] Kim WJ, Hong SI, Kim YS, Min SH, Jeong HT, Lee JD. Texture development and its effect on mechanical properties of an AZ61 Mg alloy fabricated by equal channel angular pressing. *Acta Mater* 2003;51:3293-307.
- [23] Agnew SR, Horton JA, Lillo TM, Brown DW. Enhanced ductility in strongly textured magnesium produced by equal channel angular processing. *Scripta Mater* 2004;50:377-81.
- [24] Kim WJ, Lee JB, Kim WY, Jeong HT, Jeong HG. Microstructure and mechanical properties of Mg-Al-Zn alloy sheets severely deformed by asymmetrical rolling. *Scripta Mater* 2007;56:309-12.
- [25] Kim WJ, Lee YG. High-strength Mg-Al-Ca alloy with ultrafine grain size sensitive to strain rate. *Mater Sci Eng A* 2011;528:2062-6.
- [26] Xu C, Xu SW, Zheng MY, Wu K, Wang ED, Kamado S, et al. Microstructures and mechanical properties of high-strength Mg-Gd-Y-Zn-Zr alloy sheets processed by severe hot rolling. *J Alloys Compd* 2012;524:46-52.

- [27] Xu SW, Oh-Ishi K, Kamado S, Uchida F, Homma T, Hono K. High-strength extruded Mg-Al-Ca-Mn alloy. *Scripta Mater* 2011;65:269-72.
- [28] Leng Z, Zhang JH, Zhang ML, Liu XH, Zhan HB, Wu RZ. Microstructure and high mechanical properties of Mg-9RY-4Zn (RY: Y-rich misch metal) alloy with long period stacking ordered phase. *Mater Sci Eng A* 2012;540:38-45.
- [29] Mora E, Garces G, Onorbe E, Perez P, Adeva P. High-strength Mg-Zn-Y alloys produced by powder metallurgy. *Scripta Mater* 2009;60:776-9.
- [30] Gunde P, Hanzi AC, Sologubenko AS, Uggowitzner PJ. High-strength magnesium alloys for degradable implant applications. *Mater Sci Eng A* 2011;528:1047-54.
- [31] Somekawa H, Mukai T. High strength and fracture toughness balance on the extruded Mg-Ca-Zn alloy. *Mater Sci Eng A* 2007;459:366-70.
- [32] Wang JL, Dong HW, Wang LD, Wu YM, Wang LM. Effect of hot rolling on the microstructure and mechanical properties of Mg-5Al-0.3Mn-2Nd alloy. *J Alloys Compd* 2010;507:178-83.
- [33] Xu SW, Zheng MY, Kamado S, Wu K, Wang GJ, Lv XY. Dynamic microstructural changes during hot extrusion and mechanical properties of a Mg-5.0 Zn-0.9 Y-0.16 Zr (wt.%) alloy. *Mater Sci Eng A* 2011;528:4055-67.
- [34] Fang DQ, Bi GL, Wang LM, Li GY, Jiang ZH. Microstructures and mechanical properties of Mg-2Y-1Mn-1-2Nd alloys fabricated by extrusion. *Mater Sci Eng A* 2010;527:4383-8.
- [35] Xiao WL, Jia SS, Wang J, Wu YM, Wang LM. Effects of cerium on the microstructure and mechanical properties of Mg-20Zn-8Al alloy. *Mater Sci Eng A* 2008;474:317-22.

- [36] Peng QM, Dong HW, Tian YJ, Zhang HJ. Effect of backward extrusion on microstructure and mechanical properties of Mg-Gd based alloy. *Mater Sci Eng A* 2012;532:443-8.
- [37] Zhang JH, Liu SJ, Leng Z, Liu XH, Niu ZY, Zhang ML, et al. Structure stability and mechanical properties of high-pressure die-cast Mg-Al-La-Y-based alloy. *Mater Sci Eng A* 2012;531:70-5.
- [38] Homma T, Hirawatari S, Sunohara H, Kamado S. Room and elevated temperature mechanical properties in the as-extruded Mg-Al-Ca-Mn alloys. *Mater Sci Eng A* 2012;539:163-9.
- [39] Miura H, Maruoka T, Yang X, Jonas JJ. Microstructure and mechanical properties of multi-directionally forged Mg-Al-Zn alloy. *Scripta Mater* 2012;66:49-51.
- [40] Zhang BP, Geng L, Huang LJ, Zhang XX, Dong CC. Enhanced mechanical properties in fine-grained Mg-1.0Zn-0.5Ca alloys prepared by extrusion at different temperatures. *Scripta Mater* 2010;63:1024-7.
- [41] Yang CW, Lui TS, Chen LH, Hung HE. Tensile mechanical properties and failure behaviors with the ductile-to-brittle transition of the alpha plus beta-type Mg-Li-Al-Zn alloy. *Scripta Mater* 2009;61:1141-4.
- [42] Hou XL, Cao ZY, Wang LD, Xu SW, Kamado S, Wang LM. Microstructure and mechanical properties of extruded Mg-8Gd-2Y-1Nd-0.3Zn-0.6Zr alloy. *Mater Sci Eng A* 2011;528:7805-10.
- [43] Liu HB, Qi GH, Ma YT, Hao H, Jia F, Ji SH, et al. Microstructure and mechanical property of Mg-2.0Ga alloys. *Mater Sci Eng A* 2009;526:7-10.

- [44] Zhang BP, Wang Y, Geng L, Lu CX. Effects of calcium on texture and mechanical properties of hot-extruded Mg-Zn-Ca alloys. *Mater Sci Eng A* 2012;539:56-60.
- [45] Kim WJ, Lee HW, Yoo SJ, Park YB. Texture and mechanical properties of ultrafine-grained Mg-3Al-1Zn alloy sheets prepared by high-ratio differential speed rolling. *Mater Sci Eng A* 2011;528:874-9.
- [46] Miao Q, Hu LX, Wang GJ, Wang ED. Fabrication of excellent mechanical properties AZ31 magnesium alloy sheets by conventional rolling and subsequent annealing. *Mater Sci Eng A* 2011;528:6694-701.
- [47] Zhang JH, Liu K, Fang DQ, Qiu X, Yu P, Tang DX, et al. Microstructures, mechanical properties and corrosion behavior of high-pressure die-cast Mg-4Al-0.4Mn-xPr (x=1, 2, 4, 6) alloys. *J Alloys Compd* 2009;480:810-9.
- [48] Yang J, Wang LD, Wang LM, Zhang HJ. Microstructures and mechanical properties of the Mg-4.5Zn-xGd (x = 0, 2, 3 and 5) alloys. *J Alloys Compd* 2008;459:274-80.
- [49] Lim HK, Kim DH, Lee JY, Kim WT, Kim DH. Effects of alloying elements on microstructures and mechanical properties of wrought Mg-MM-Sn alloy. *J Alloys Compd* 2009;468:308-14.
- [50] Son HT, Lee JB, Jeong HG, Konno TJ. Effects of Al and Zn additions on mechanical properties and precipitation behaviors of Mg-Sn alloy system. *Mater Lett* 2011;65:1966-9.
- [51] Xu DK, Liu L, Xu YB, Han EH. The influence of element Y on the mechanical properties of the as-extruded Mg-Zn-Y-Zr alloys. *J Alloys Compd* 2006;426:155-61.
- [52] Xu DK, Liu L, Xu YB, Han EH. The effect of precipitates on the mechanical properties of ZK60-Y alloy. *Mater Sci Eng A* 2006;420:322-32.

- [53] Watanabe H, Yamaguchi M, Takigawa Y, Higashi K. Mechanical properties of Mg-Al-Ca alloy processed by hot extrusion. *Mater Sci Eng A* 2007;454:384-8.
- [54] Yang J, Wang JL, Wang LD, Wu YM, Wang LM, Zhang HJ. Microstructure and mechanical properties of Mg-4.5Zn-xNd (x=0, 1 and 2, wt%) alloys. *Mater Sci Eng A* 2008;479:339-44.
- [55] Li B, Yan PF, Sui ML, Ma E. Transmission electron microscopy study of stacking faults and their interaction with pyramidal dislocations in deformed Mg. *Acta Mater* 2010;58:173-9.
- [56] Smola B, Stulikova I, Pelcova J, Mordike BL. Significance of stable and metastable phases in high temperature creep resistant magnesium-rare earth base alloys. *J Alloys Compd* 2004;378:196-201.
- [57] Sandlobes S, Friak M, Zaefferer S, Dick A, Yi S, Letzig D, et al. The relation between ductility and stacking fault energies in Mg and Mg-Y alloys. *Acta Mater* 2012;60:3011-21.
- [58] Liao XZ, Srinivasan SG, Zhao YH, Baskes MI, Zhu YT, Zhou F, et al. Formation mechanism of wide stacking faults in nanocrystalline Al. *Appl Phys Lett* 2004;84:3564-6.
- [59] Zhu YT, Wu XL, Liao XZ, Narayan J, Kecskes LJ, Mathaudhu SN. Dislocation-twin interactions in nanocrystalline fcc metals. *Acta Mater* 2011;59:812-21.

## **CHAPTER 4: Investigation of Strengthening Mechanisms in an Ultrastrong Mg Alloy Processed by Hot Rolling**

### 4.1 Introduction

In the previous section, we made a breakthrough in producing an ultrastrong Mg-8.5Gd-2.3Y-1.8Ag-0.4Zr (wt.%) alloy processed by conventional hot rolling. As the rolling strain increasing, the strength of the Mg-8.5Gd-2.3Y-1.8Ag-0.4Zr alloy increased dramatically without a loss of ductility and an unprecedented ultrahigh strength, ~600 MPa of UTS and ~575 MPa of YS, were recorded. The main strengthening mechanism was demonstrated to be the high density of stacking faults (SFs) inside the grains, which is a new strengthening mechanism in hcp metals.

Meanwhile, during solution treatment and the following hot rolling process, solid solution, grain refinement, precipitation and texture evolution took place in Mg-8.5Gd-2.3Y-1.8Ag-0.4Zr specimens. These might serve as possible strengthening mechanisms contributing to the unprecedented ultrahigh strength.

To the best of the authors' knowledge, prediction and calculation strengthening contributions are always challenging and the results could be reasonably acceptable only if the appropriate models and parameters are carefully identified. In this article, the models and parameters were identified carefully with the following criteria: (1) the parameters, such as shear modulus, are extracted from the published references in which the materials under investigation possessed the same composition or at least had the same major alloying elements as Mg-8.5Gd-2.3Y-1.8Ag-0.4Zr (wt.%) alloy and (2) the models, such as Hall-Patch equation and Orowan strengthening models, were chosen based on the reported

experimental circumstances which were almost identical to our current research. With all of our work, the results can be a solid reference to support our conclusion that introducing high density of SFs was a main strengthening mechanism contributed to the unprecedented ultrahigh strength.

## 4.2 Prediction and Calculation of Various Strengthening Contribution

The details about casting of Mg-8.5Gd-2.3Y-1.8Ag-0.4Zr (wt.%) alloy ingot and hot rolling experiment can be found in reference [1]. Hereafter in the article, we will refer the possible strengthening mechanisms, other than high density of SFs strengthening, as (1) grain boundary strengthening,  $\sigma_1$ , (2) solid solution hardening,  $\sigma_2$ , (3) precipitates hardening,  $\sigma_3$  and (4) strong texture strengthening,  $\sigma_4$ . All of the calculations are based on the rolled Mg sample with thickness reduction of 88%.

### 4.2.1 Grain Boundary Strengthening, $\sigma_1$

Figure 4.1 shows OM images of as-cast, solution treatment (T4 treatment) and 88% hot rolled Mg-8.5Gd-2.3Y-2.0Ag-0.4Zr alloy. The mean grain size of casting sample was  $\sim 40 \mu\text{m}$  (Figure 4.1a) which was increased to  $\sim 61 \mu\text{m}$  after T4 treatment at  $500^\circ\text{C}$  for 12 hours (Figure 4.1b). Dynamic recrystallization (DRX) took place in the 88% hot rolled specimen and grains were refined to an equiaxial microstructure with average grain size of  $\sim 13 \mu\text{m}$  as seen in Figure 4.1c. Grain refinement introduces high concentration of grain boundaries (GBs) and consequently improves the yield strength according to empirical Hall-Petch equation:

$$\sigma_y = \sigma_0 + Kd^{-1/2} \quad (4.1)$$

where  $\sigma_0$  is the intrinsic resistance of the lattice to dislocation motion, which is 46.5 MPa for Mg-Gd alloys [2]), K is a constant which is  $164 \text{ MPa} \cdot \mu\text{m}^{1/2}$  for extruded-T5 Mg-Gd-Y

alloys [3] and  $d$  is the average grain size of  $\sim 13 \mu\text{m}$  for the as-rolled specimen in current experiment. The calculated grain boundary strengthening contribution  $\sigma_1 = 88.8 \text{ MPa}$ . Therefore, grain size of 88% hot rolled Mg alloy was not refined to a level (ultrafine scale) where GB strengthening can be a dominant contribution to ultrahigh yield strength in this report.

#### 4.2.2 Solid Solution Hardening, $\sigma_2$

As the cast Mg-8.5Gd-2.3Y-2.0Ag-0.4Zr samples T4 treated at  $500 \text{ }^\circ\text{C}$  for 12 hours, most of the intergranular precipitates on the grain boundaries (Figure 4.1a) are dissolved into matrix (Figure 4.1a) and the matrix is a supersaturated solid solution (S.S.S.S). The solute atoms can either collect on dislocations at rest (dislocation locking) or act on the moving dislocations (dislocation friction) by which extra work or stress needs to be provided in order for a dislocation to move [4]. These direct interactions between solute atoms and dislocations were considered as mechanisms of solid-solution hardening. However, the hot rolled Mg-8.5Gd-2.3Y-1.8Ag-0.4Zr (wt.%) samples were not in a S.S.S.S. status since intensive precipitate nucleation and growth occurred as shown in Figure 4.2. The contribution to the yield strength of solid solution atoms can be expressed by Eq. (4.2)[5]:

$$\sigma_y = \sigma_u + \frac{3.1\varepsilon GC^{1/2}}{700} \quad (4.2)$$

where  $G$  is the shear modulus of the matrix ( $18.07 \text{ GPa}$  of Mg-10Gd-3Y-0.4Zr [6]),  $\varepsilon$  is an experimental constant ( $0.74$  for Mg–Gd series alloy [7]) and  $\sigma_u$  is the tensile yield strength (TYS) of pure Mg ( $\sigma_u = 21 \text{ MPa}$ [5]).  $C$  is the concentration of the solute in atomic

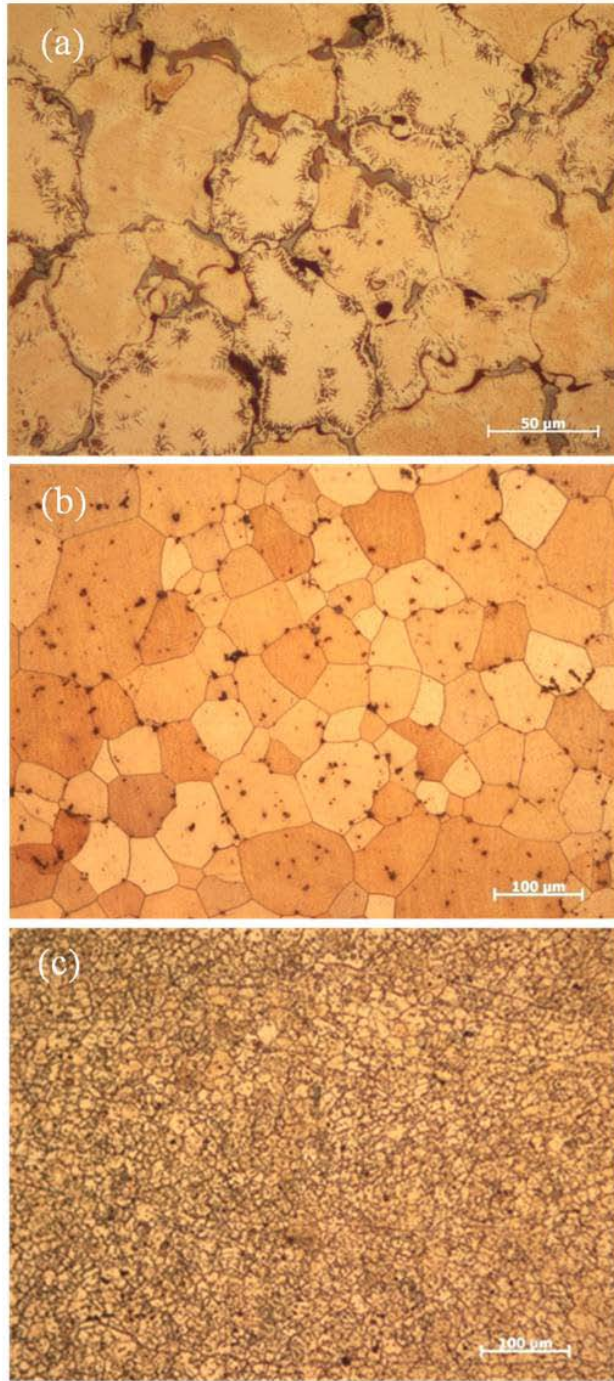


**Figure 4.1** OM images of Mg-8.5Gd-2.3Y-2.0Ag-0.4Zr alloy: (a) as-cast, (b) T4 treated and (c) T4 treated+450 °C 88% hot rolled.

**Table 4.1** EDS result of the concentration of the solutes (at.%) in matrix of 450°C 88% rolled Mg-8.5Gd-2.3Y-2.0Ag-0.4Zr sample.

<b>Element</b>	<b>Mg</b>	<b>Gd</b>	<b>Y</b>	<b>Ag</b>	<b>Zr</b>
<b>Concentration of solutes (at. %)</b>	<b>96.82</b>	<b>1.551</b>	<b>0.7988</b>	<b>0.7775</b>	<b>0.0550</b>

percentage, which is 3.18% (at%) from EDS analysis as shown in Table 4.1. Therefore, the solid solution strengthening contribution is calculated to be  $\sigma_2=31.6\text{MPa}$  which means the solid solution strengthening mechanism is not the main mechanism accounting for the ultrahigh strength.

#### 4.2.3 Precipitates Hardening, $\sigma_3$

Figure 4.2 shows the TEM image of the precipitates in 88% hot rolled Mg-8.5Gd-2.3Y-2.0Ag-0.4Zr sample. It is obvious that dynamic precipitation took place intensively in Mg-8.5Gd-2.3Y-1.8Ag-0.4Zr (wt.%) alloy during hot rolling. The effects of precipitates on the yield strength of materials can be divided into (i) dislocation-particle interaction by the Orowan process, (ii) dislocation generation due to a difference in thermal expansion between a matrix and a particle and (iii) dislocation generation required geometrically during deformation [8].

##### 4.2.3.1 Dislocation-particle Interaction by Orowan Stress

Precipitate hardening can be achieved by introducing a particular dispersion of obstacles to dislocation movement, the particular dispersion being achieved by a second phase

precipitation process [9]. When a dislocation moves and encounters a hard, undeformable second phase precipitate, dislocation releases at higher stresses may occur by Orowan looping [10]. Figure 4.3 shows an Orowan loop as dislocation bypasses two adjacent precipitates. In current research, all precipitates, except for those indicated by white arrows as shown in Figure 4.2, could be approximately regarded as spherical particles and the average diameter of these precipitates,  $d$ , is  $0.96 \mu\text{m}$ . The calculation details of volume fraction and mean diameter of precipitates can be found in Appendix B. Since the most of precipitates are spherical particles without orientation relationship with the matrix and no shear deformation of precipitates has been observed, the following equation could be used to calculate the Orowan stress for dislocation to by-pass these obstacles [10]:

$$\Delta\sigma_{\text{orowan}} = \frac{Gb}{2\pi\sqrt{1-\nu}\left(\frac{0.779}{\sqrt{f}} - 0.785\right)d} \ln \frac{0.785d}{b} \quad (4.3)$$

where  $G$  is the shear modulus of the matrix ( $18.07 \text{ GPa}$  of  $\text{Mg-10Gd-3Y-0.4Zr}$  [6]), Burger vector  $b=0.321 \text{ nm}$  for  $\langle a \rangle$  dislocation,  $d$  is the average diameter of precipitates,  $\sim 0.96 \mu\text{m}$  and Poisson's ratio  $\nu=0.35$  [5]. In the circumstance that the dispersion of precipitates is random, the volume fraction of precipitates,  $f$ , can be assumed to be equal to the area fraction of the precipitates [11], which is  $3.37\%$  in this experiment. Therefore, the Orowan stress for dislocation to by-pass precipitates, in our research, is only  $2.7 \text{ MPa}$ .

#### 4.2.3.2 Dislocation Generation due to a Difference in Thermal Expansion

High density of dislocations generated by a difference in thermal expansion between two components can cause an increase in yield stress [8]. Assuming that dislocations are

generated homogeneously throughout a matrix and that all thermal stresses are relieved by the generation of dislocations, an increase in yield stress due to a difference in thermal expansion between a matrix and a particle may be given by [5, 12]:

$$\Delta\sigma_{TE} = \alpha Gb \left( \frac{12\Delta T \Delta C f_v}{bd_t} \right)^{1/2} \quad (4.4)$$

$\Delta T$ , 430 K in this research, is the temperature change during cooling of the rolled sample from 450°C to room temperature.  $\Delta C$  is the difference in the thermal expansion coefficients between the two components where  $C_{Mg} = 2.61 \times 10^{-5} \text{ K}^{-1}$  [7]. The constant  $\alpha$  is between 0.5 and 1.25 [5]. By choosing  $\alpha=1.25$  and  $C_{precipitat} = 0$ , the maximum stress from thermal expansion is 28.0 MPa.

#### 4.2.3.3 Dislocation Generation Required Geometrically during Deformation.

During plastic deformation, incompatibility between a matrix and a particle causes the generation of geometrically necessary dislocations, which results in an increased strain hardening rate of a particle-reinforced metal [7]. The contribution associated with the generation of this type of dislocations can be written as [5, 7]:

$$\Delta\sigma_g = \alpha Gb \left( \frac{8f_v \gamma}{bd_t} \right)^{1/2} \quad (4.5)$$

where  $\gamma$  is the shear strain calculated with the use of the Taylor factor  $M$ , according  $\epsilon = \gamma/M$  [13]. The Taylor factor  $M$  for hcp is 6.5 [14] and  $\epsilon$  is 0.2% based on the assumption that the particles are non shearable. Substituting all the parameters,  $\Delta\sigma_g = 24.6 \text{ MPa}$  can be obtained. So the total stress increase from precipitates hardening is  $\sigma_3 = 2.7 + 28.0 + 24.6 = 55.3 \text{ MPa}$ .

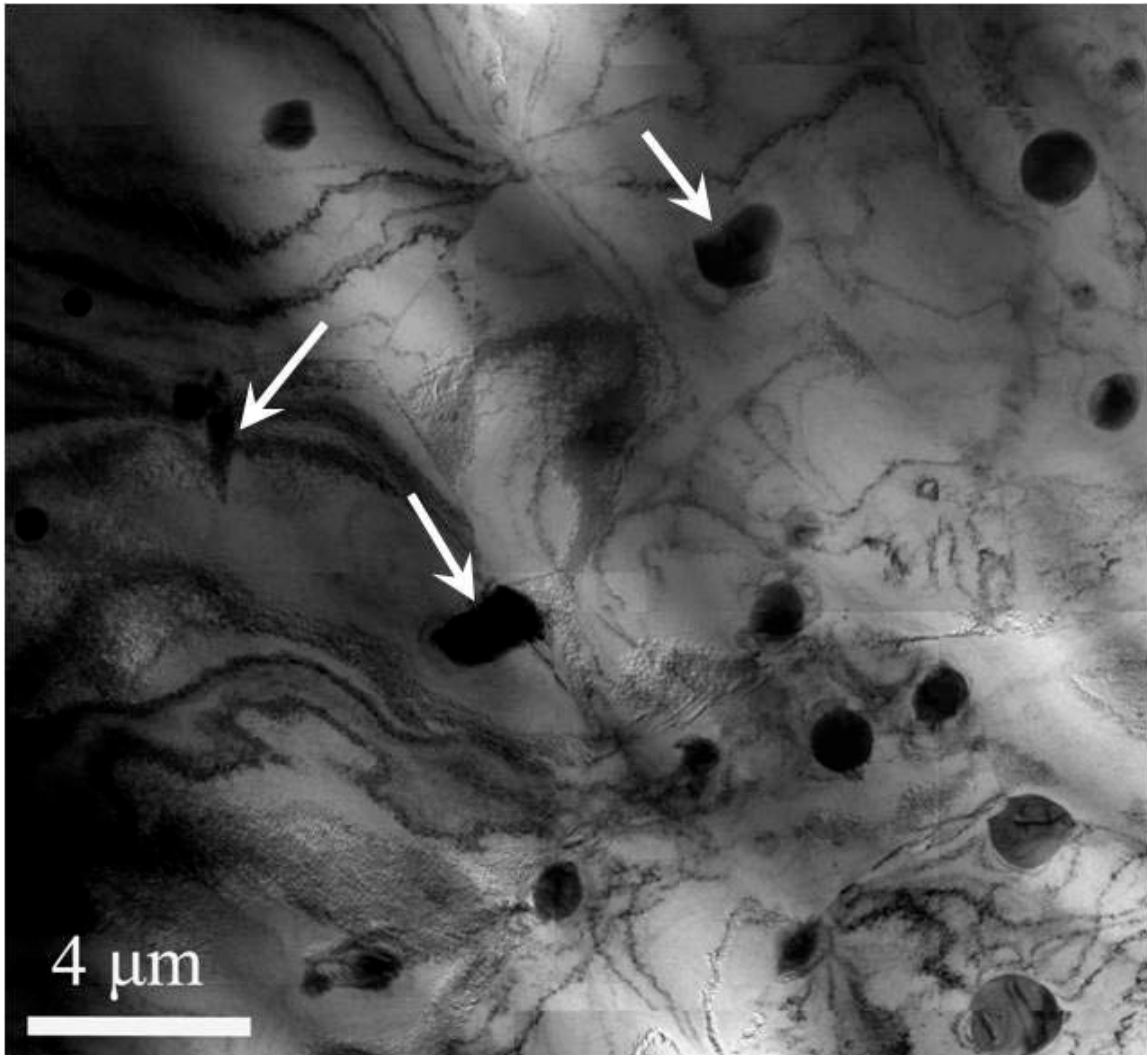


**Figure 4.2** TEM image show the distribution of precipitates in 88% hot rolled Mg-8.5Gd-2.3Y-2.0Ag-0.4Zr sample. Non-spherical precipitates are marked by white arrows.

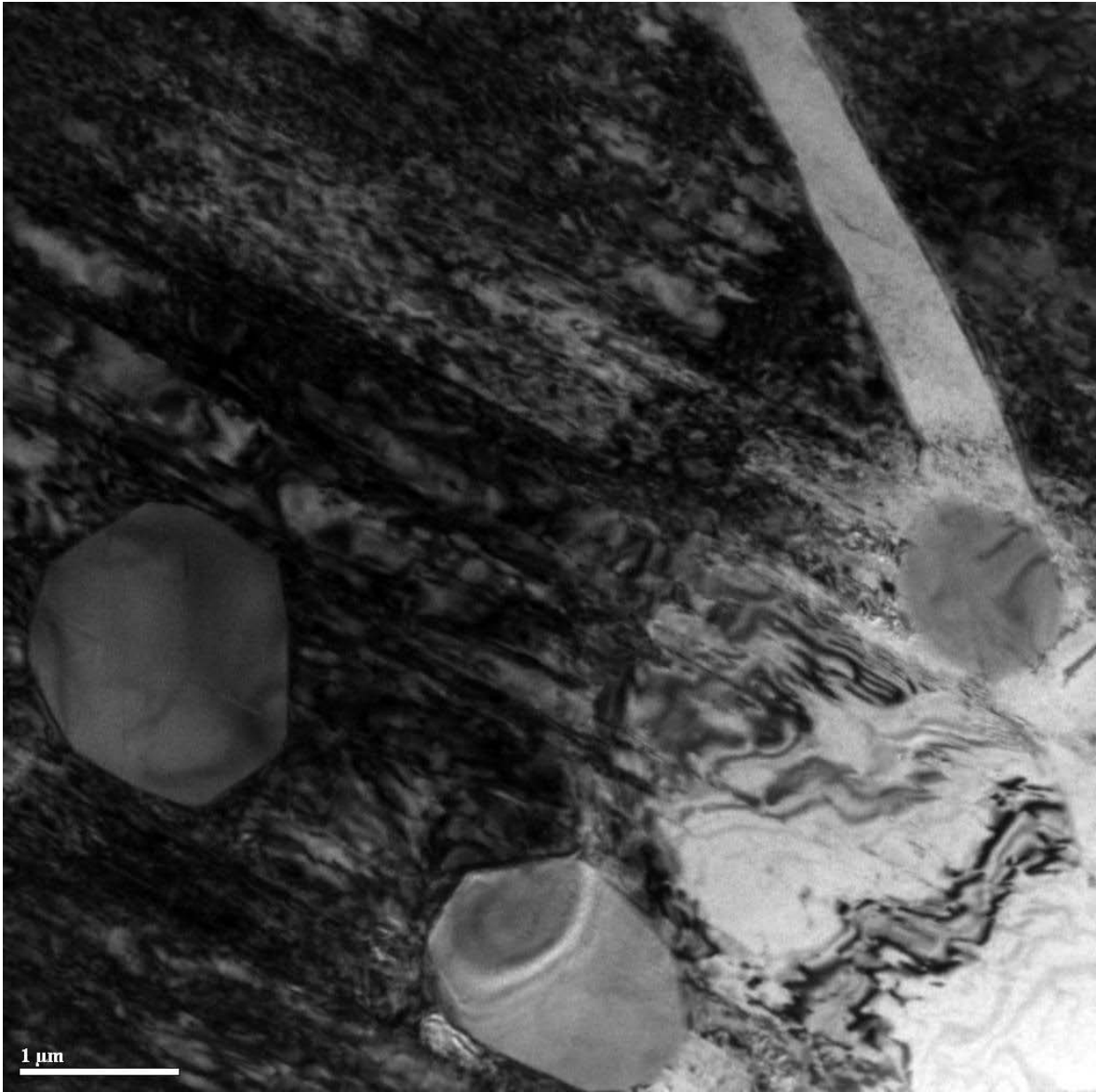


**Figure 4.3** TEM image shows dislocations trapped around precipitates.

#### 4.2.4 Strong Texture Strengthening, $\sigma_4$

In current research, strong basal texture with the basal plane (0002) parallel to rolling direction was introduced in the Mg-8.5Gd-2.3Y-1.8Ag-0.4Zr samples as the rolling thickness reduction proceeded to > 50% (Figure 4.4). Basal plane texture was demonstrated to be effective on altering ductility and strength of Mg alloys [15, 16]. When rolled samples were tensile tested in the direction perpendicular to the basal plane normal, the c-axis was constrained and extension twinning was not favorable. Therefore, non basal slip can be a mode of deformation to accommodate a certain amount of plastic deformation and consequently improve or maintain a reasonable good ductility [16-18]. Since the strong basal textures were introduced in the rolled samples as the rolling thickness reduction > 50%, the texture strengthening did not account for the strength improvement, from 55% rolled samples to 88% rolled samples, as shown in the Fig. 3.1. It was demonstrated that strong basal texture strengthening accounted for only ~15% to 20% of the tensile strength of a Mg alloy [19]. So in this research, the stress increase due to strong basal texture was  $\sigma_4=86.3$  MPa to 115 MPa.

#### 4.3 Summary

The yield strength contribution from grain boundary strengthening,  $\sigma_1$ , solid solution hardening,  $\sigma_2$ , precipitates hardening,  $\sigma_3$  and strong texture strengthening,  $\sigma_4$ , totally account for 262.0 MPa to 290.7 MPa. It should be pointed out that the calculated strengthening values from various strengthening mechanisms might be slightly different from the real values. However, our calculations can give the general strengthening values, from the strengthening mechanisms other than nano-spaced SFs, that demonstrate the nano-spaced SFs was the main strengthening factor in this research.

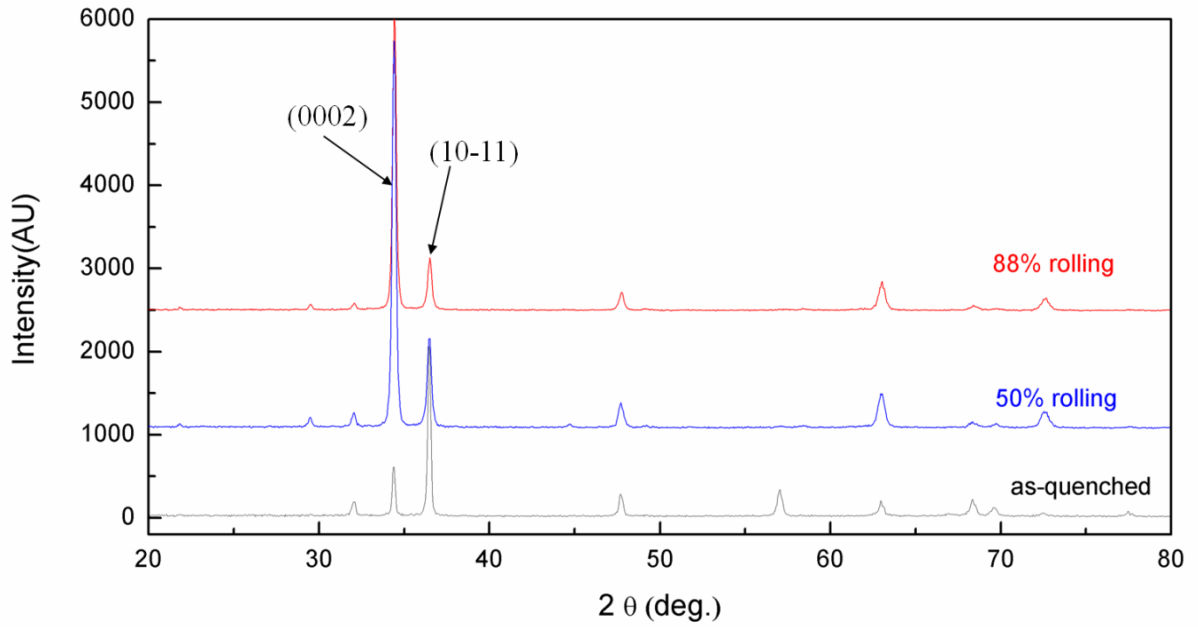


**Figure 4.4** XRD patterns of as quenched and hot rolled samples shows the texture evolution.

## REFERENCES

- [1] Wang Q, Chen J, Zhao Z, He S. Microstructure and super high strength of cast Mg-8.5Gd-2.3Y-1.8Ag-0.4Zr alloy. *Materials Science and Engineering: A* 2010;528:323-8.
- [2] Gao L, Chen R, Han E. Microstructure and strengthening mechanisms of a cast Mg-1.48Gd-1.13Y-0.16Zr (at.%) alloy. *J Mater Sci* 2009;44:4443-54.
- [3] He SM, Zeng XQ, Peng LM, Gao X, Nie JF, Ding WJ. Microstructure and strengthening mechanism of high strength Mg-10Gd-2Y-0.5Zr alloy. *J Alloy Compd* 2007;427:316-23.
- [4] Haasen P. Mechanical properties of solid solutions. In: Cahn RW HP, editor. *Physical Metallurgy*. 4th ed. North Holland: Elsevier Ltd; 1996. p. 2016.
- [5] Zheng L, Liu C, Wan Y, Yang P, Shu X. Microstructures and mechanical properties of Mg-10Gd-6Y-2Zn-0.6Zr(wt.%) alloy. *J Alloy Compd* 2011;509:8832-9.
- [6] Wang QD. Unpublished data.
- [7] Yang Z, Li JP, Guo YC, Liu T, Xia F, Zeng ZW, et al. Precipitation process and effect on mechanical properties of Mg-9Gd-3Y-0.6Zn-0.5Zr alloy. *Materials Science and Engineering: A* 2007;454-455:274-80.
- [8] Mabuchi M, Higashi K. Strengthening mechanisms of Mg-Si alloys. *Acta Materialia* 1996;44:4611-8.
- [9] Gladman T. Precipitation hardening in metals. *Mater Sci Tech-Lond* 1999;15:30-6.
- [10] Nie JF. Effects of precipitate shape and orientation on dispersion strengthening in magnesium alloys. *Scripta Materialia* 2003;48:1009-15.
- [11] Martin JW. *Micromechanisms in particle-hardened alloys*. 1st ed. UK: Cambridge University Press; 1980.

- [12] Luster JW, Thumann M, Baumann R. Mechanical properties of aluminium alloy 6061- $\text{Al}_2\text{O}_3$  composites. *Mater Sci Tech-Lond* 1993;9:853-62.
- [13] Dillamore IL, Roberts JG, Bush AC. Occurrence of shear bands in heavily rolled cubic metals. *Metal Science* 1979; 13:73-7.
- [14] Armstrong R, Codd I, Douthwaite RM, Petch NJ. The plastic deformation of polycrystalline aggregates, *Phil. Mag.* 1962; 7: 45-58.
- [15] Razavi SM, Foley DC, Karaman I, Hartwig KT, Duygulu O, Kecskes LJ, et al. Effect of grain size on prismatic slip in Mg–3Al–1Zn alloy. *Scripta Materialia* 2012;67:439-42.
- [16] Jain A, Duygulu O, Brown DW, Tomé CN, Agnew SR. Grain size effects on the tensile properties and deformation mechanisms of a magnesium alloy, AZ31B, sheet. *Materials Science and Engineering: A* 2008;486:545-55.
- [17] Yuan W, Mishra RS, Carlson B, Mishra RK, Verma R, Kubic R. Effect of texture on the mechanical behavior of ultrafine grained magnesium alloy. *Scripta Materialia* 2011;64:580-3.
- [18] Ulacia I, Dudamell NV, Gálvez F, Yi S, Pérez-Prado MT, Hurtado I. Mechanical behavior and microstructural evolution of a Mg AZ31 sheet at dynamic strain rates. *Acta Materialia* 2010;58:2988-98.
- [19] Kaneko J SM, Numa M, Nishikawa Y, Takada H. Effect of texture on the mechanical properties and formability of magnesium wrought materials. *J Jpn I Met* 2000;64:141-7.

## CHAPTER 5: Strengthening Mechanism of Mg alloy by Nano-Spaced SFs

### 5.1 Introduction

SF is one type of coherent planar defects in metals, especially for those having low stacking fault energy [1-4]. In Mg alloys, adding Gd and Y elements can lower the stacking fault energy (SFE) and make a full dislocation easily split into two partials [5, 6]. During plastic deformation, the partials tend to glide on the basal plane in opposite directions to form wider planer stacking fault ribbon [4]. The formation mechanism of a SF in hcp Mg alloy has some characteristics analogous to that of twinning in fcc metals. Both SF and twinning formations involve the dissociation of full dislocations and motion of partial dislocations on close-packed plane. The only difference is that multiple slips of partials on successive planes are needed to form a twinning, other than the one partial slip that is sufficient for a SF formation. Since nanoscale coherent internal twin boundaries can sustain more pronounced strain hardening [7-10], we speculate that nanoscale SFs could also be able to provide the same effect in impeding dislocation movement and retain the materials with moderate or high strain hardening rate for the following reasons.

First, as nano-spaced SFs were introduced in the material, the crystal lattice would be distorted, which was attributed to frequent atomic stacking sequence changes. In addition, SFs could introduce certain degree of crystallographic disregistry, even though not as great as that of grain boundary, between adjacent regions of the atomic lattice [9]. Either the lattice distortion or crystallographic disregistry can be regarded as barriers for dislocation motion. Second, when a high density of SFs was introduced in the grain interior, there are complex stress fields, due to the superposition of the stress field from individual partials, existing in

the grain interior. The stress field will exert either an attractive or repelling force as dislocations (basal dislocations or non-basal dislocations) move closer to the partials bounding the pre-existing SFs. The attractive or repelling force serves as an extra force for the basal dislocation to overcome in order to move on slip plane. Therefore these nano-spaced SFs could be barriers to inhibit dislocation motion.

In chapter 3, we experimentally found that SFs were effective in blocking dislocation motion and retaining strain hardening capability of the Mg alloy. Introducing nano-spaced SFs alloy can render a 88% rolled Mg-8.5Gd-2.3Y-1.8Ag-0.4Zr (wt.%) alloy with ultrahigh strength (yield strength: ~575 MPa, ultimate strength: ~600 MPa) and maintaining moderate ductility (uniform elongation: ~5.2 %). The yield strengths of hot rolled samples increased linearly as the spacing between adjacent SFs decreased and meanwhile, the ductility remained a constant level without severe loss. These interesting findings experimentally demonstrated that introducing high density of SFs could be a new strategy to strengthen Mg alloy without significant loss of ductility.

In this chapter, we first identified the types of dislocations (basal dislocations:  $\langle a \rangle$  or non-basal dislocations:  $\langle c+a \rangle$  and  $\langle c \rangle$ ), which were activated during tensile testing of the hot rolled Mg-8.5Gd-2.3Y-1.8Ag-0.4Zr (wt.%) sample. Then, the interaction models of dislocations vs. SFs were proposed and the interaction force between the identified dislocations and SFs will be derived and calculated based on the classical Peach-Koehler formula [9]. Our theoretical analysis shown that the interaction forces between dislocations (both basal and non basal) and SFs were all proportional to the reciprocal of the spacing between adjacent SFs which could be solid supports for our previous experimental findings

in chapter 3. This was the first attempt to fundamentally calculate the interaction forces between SFs and dislocations in hcp Mg alloy based on the stress fields of the defects. The theoretical analysis, in this research, as well as the previous experimental investigation of the new strengthening mechanism, nano-spaced SFs, are significantly important for alloys (hcp and other structures) development, processing and applications.

## 5.2 Identification of Dislocations Activated during Tensile Test

In this research, the solution treated Mg-8.5Gd-2.3Y-1.8Ag-0.4Zr (wt.%) alloys were hot rolled with thickness reduction up to 88%. The details about the solution treatment, the hot rolling experiments as well as the room temperature tensile tests can be found in chapter 2. The dominant defects in 88% rolled Mg-alloy sample are high density of SFs (Fig. 5.1a) with mean spacing of ~16 nm. As the tensile test sample was pulled to failure at room temperature, the unique microstructure of nano-spaced SFs was replaced by high densities of dislocations as shown in Fig. 5.1b.

Fig. 5.1 b-d shown TEM images of the dislocations, in the 88% rolled sample after tensile testing, using two beams technique. According to the visibility criterion,  $g \cdot b \neq 0$ , the  $\langle a \rangle$  dislocation or dissociated  $\langle a \rangle$  dislocations (hereafter named basal dislocations) should be visible in TEM image when the incident beam tilts to the two-beams condition with  $g = [11\bar{2}0]$ . The  $\langle c \rangle$  dislocation or  $\langle c \rangle$  component of a non-basal dislocation with should be visible in the TEM image with  $g = [0002]$ . And  $\langle c+a \rangle$  dislocation should be visible in both  $g = [11\bar{2}0]$  and  $g = [0002]$  conditions [11, 12]. Therefore, as indicated by arrows in Fig. 5.1

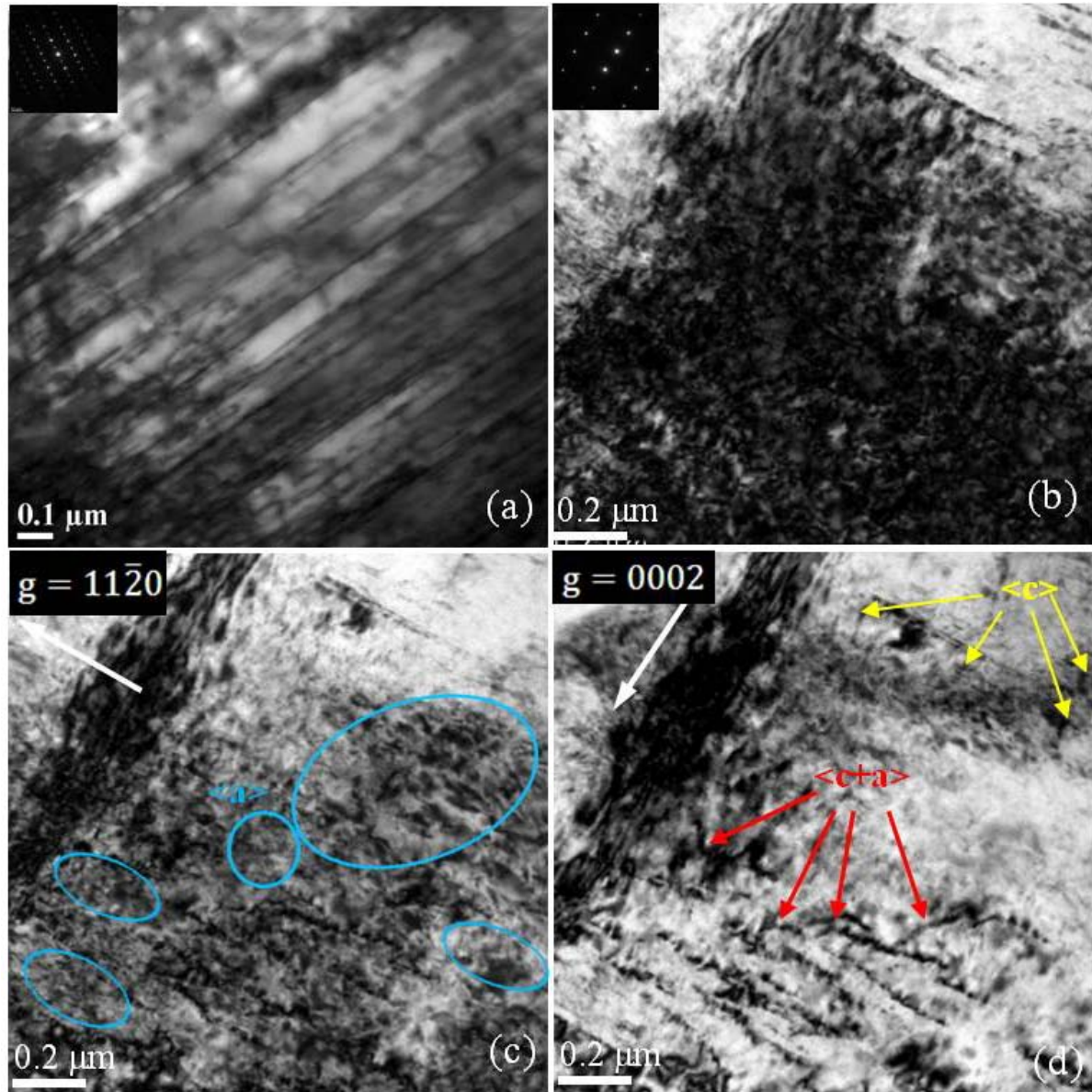


**Figure 5.1** TEM image of Mg-8.5Gd-2.3Y-1.8Ag-0.4Zr (wt.%) alloy samples: (a) 88% hot rolled before tensile test, (b) 88% hot rolled after tensile test, (c) and (d) two-beam bright field images with different  $g$  vectors indicated the white arrows.

c and d, both basal dislocations and non basal dislocations existed in tensile tested Mg-alloy sample. In addition,  $\langle c \rangle$  dislocation were also observed, which rarely existed in Mg alloys [12].

In hcp Mg alloys, the basal dislocation,  $\langle a \rangle$ , usually slips on the close-packed basal plane (slip system:  $\frac{1}{3}\langle 11\bar{2}0 \rangle \{0001\}$ ) and the non basal dislocation,  $\langle c+a \rangle$ , usually slips on the pyramidal plane (slip system:  $\frac{1}{3}\langle 11\bar{2}\bar{3} \rangle \{11\bar{2}2\}$ ) [11, 13]. During room temperature tensile test in current research, basal and non basal dislocations can either (1) accumulate around SFs boundaries and accommodate increased strain hardening [14] or (2) cut or interact with SFs in order to move and facilitate plastic deformation. In the following sections, we will discuss interactions of SFs with (1) basal plane  $\langle a \rangle$  dislocation and (2)  $\langle c \rangle$  dislocation on  $\{10\bar{1}0\}$  plane. Since the activities of  $\langle c+a \rangle$  can be crystallographically decomposed into  $\langle a \rangle$  dislocation moving on basal plane and  $\langle c \rangle$  dislocation moving on  $\{10\bar{1}0\}$  plane, the interaction force between SFs and  $\langle c+a \rangle$  dislocations can be added by the interaction forces between SFs and  $\langle a \rangle$  and  $\langle c \rangle$  dislocations.

### 5.3 Interaction between SFs and $\langle a \rangle$ Dislocation on Basal Plane

Fig. 5.2(a) is the schematic illustration of a moving dissociated  $\langle a \rangle$  dislocation interacting with a pair of adjacent SFs. This illustration was drawn based on some assumptions that will be discussed later. The dissociated  $\langle a \rangle$  dislocation is a planer stacking fault (highlighted in blue color) bounded by two partial dislocations,  $\bar{b}_3$  and  $\bar{b}_6$ . The  $\langle a \rangle$  dislocation dissociates in the same manner as the SFs formation. The deformation SFs

ribbons are highlighted in purple, bounded by a pair of partial dislocations, dislocations,  $\bar{b}_1$  and  $\bar{b}_2$ , and,  $\bar{b}_3$  and  $\bar{b}_4$ . So the interaction force between  $\langle a \rangle$  dislocation on basal plane and SFs is actually the interaction force between partial dislocations dissociated from  $\langle a \rangle$  dislocations and partial dislocations bounding the stacking fault ribbons. When a dissociated  $\langle a \rangle$  dislocation is moving on the basal plane between adjacent SFs and encountering one of the partial dislocations, the dissociated  $\langle a \rangle$  dislocation will experience a force induced by the stress field of that partial dislocation.

For the convenience of analyzing the force between dislocations using Peach-Koehler equation[6], we will assume that (1) the  $\langle a \rangle$  full dislocation is an edge dislocation which is dissociated in two partial dislocations labeled  $\bar{b}_5$  and  $\bar{b}_6$ , in Fig. 5.2(a); (2) the sense vectors of all the dislocations are identical and parallel to each other; (3) partial dislocations  $\bar{b}_1$  and  $\bar{b}_3$  are on the same vertical plane ( $\bar{b}_3$  is right above  $\bar{b}_1$ ) and (4) the spacing distance between adjacent SFs is  $d$  and the dissociated  $\langle a \rangle$  dislocations moving on the basal plane, which is an equal distance,  $d/2$ , from each SF as shown in Fig.5.2 (b). Fig. 5.1(c) shows that the coordinate system is established as the z-axis and x-axis parallel to the sense vector,  $\bar{\xi}$ , and Burger vector,  $\bar{b}$ , of  $\langle a \rangle$  dislocation, respectively.

In order to make the derivation clear, the partial dislocations are labeled as  $\bar{b}_i$ , where  $i=1$  to 6 as shown in the Fig. 5.2(b).  $\bar{b}_1$ ,  $\bar{b}_3$  and  $\bar{b}_5$  are essentially the same with the Burger vectors of  $\bar{b}_1 = \bar{b}_3 = \bar{b}_5 = b_{1e}i + b_{1s}k$ , where  $b_{1e} = \frac{\sqrt{3}}{2}b_1$  and  $b_{1s} = -\frac{1}{2}b_1$  are the magnitude of the

edge and screw component of  $\bar{b}_1$ , respectively. The sense vector of  $\bar{b}_5$  is  $\bar{\xi}_5 = k$  which is parallel to the z-axis. The stress of dislocation  $\bar{b}_1$  exerting on dislocation  $\bar{b}_5$  is

$$\bar{\sigma}_{15} = ii\sigma_{xx} + ij\sigma_{xy} + ji\sigma_{yx} + jj\sigma_{yy} + kk\sigma_{zz} + ik\sigma_{xz} + ki\sigma_{zx} + jk\sigma_{yz} + kj\sigma_{zy} \quad (5.1)$$

From the Peach-Koehler formula, the force exerted on a unit length of dislocation  $\bar{b}_5$  due to the stress field of dislocation  $\bar{b}_1$  is  $\bar{F}_{15} = (\bar{\sigma}_{15} \cdot \bar{b}_5) \times \bar{\xi}_5$ . Substituting the  $\bar{\sigma}_{15}$  and  $\bar{b}_5$ ,

$$\bar{F}_{15} = (\bar{\sigma}_{15} \cdot \bar{b}_5) \times \bar{\xi}_5 = (\sigma_{yx}b_{1e} + \sigma_{yz}b_{1s})i - (\sigma_{xx}b_{1e} + \sigma_{xz}b_{1s})j \quad (5.2)$$

Therefore the force exerting on unit length of dislocation  $\bar{b}_5$  due to the stress field of dislocation  $\bar{b}_1$  along x(i) direction is:

$$F_{15}|_i = \sigma_{yx}b_{1e} + \sigma_{yz}b_{1s} = \frac{3\mu b_1^2}{8\pi(1-\nu)} \frac{x(x^2 - y^2)}{(x^2 + y^2)^2} + \frac{\mu b_1^2}{8\pi} \frac{x}{x^2 + y^2} \quad (5.3)$$

The same derivation procedure can be applied to obtain the force exerted on a unit length of dislocation  $\bar{b}_5$  due to the stress field of dislocation  $\bar{b}_3$  along x(i) direction is:

$$F_{35}|_i = \sigma_{yx}b_{3e} + \sigma_{yz}b_{3s} = \frac{3\mu b_1^2}{8\pi(1-\nu)} \frac{x[x^2 - (y-d)^2]}{[x^2 + (y-d)^2]^2} + \frac{\mu b_1^2}{8\pi} \frac{x}{x^2 + (y-d)^2} \quad (5.4)$$

Therefore the total force exerted on a unit length of dislocation  $\bar{b}_5$  due to the stress field of dislocation  $\bar{b}_1$  and  $\bar{b}_3$  along x(i) direction is

$$F_{total}|_i = F_{15}|_i + F_{35}|_i = \frac{3\mu b_1^2}{8\pi(1-\nu)} \frac{x(x^2 - y^2)}{(x^2 + y^2)^2} + \frac{\mu b_1^2}{8\pi} \frac{x}{x^2 + y^2} + \frac{3\mu b_1^2}{8\pi(1-\nu)} \frac{x[x^2 - (y-d)^2]}{[x^2 + (y-d)^2]^2} + \frac{\mu b_1^2}{8\pi} \frac{x}{x^2 + (y-d)^2} \quad (5.5)$$

Because the dissociated <a> dislocation moves on the basal plane, which is an equal spacing distance, d/2, from each SF, y=d/2 can be substituted in  $F_{total}|_i$ .

$$F_{total}|_i = \frac{3\mu b_1^2}{4\pi(1-\nu)} \frac{x(x^2 - \frac{1}{4}d^2)}{(x^2 + \frac{1}{4}d^2)^2} + \frac{\mu b_1^2}{4\pi} \frac{x}{x^2 + \frac{1}{4}d^2} \quad (5.6)$$

where  $\mu=18.07$  GPa is the shear modulus for Mg-8.5Gd-2.3Y-1.8Ag-0.4Zr (wt.%) alloy [15],

$$b_1 = \frac{\sqrt{3}}{3}a = 0.1853 \times 10^{-9} m, \text{ Poisson's ratio } \gamma=0.35[16].$$

By resolving this equation, the maximum interaction force  $F_{total}|_i$  is equal to  $0.1502 \frac{1}{d}$

where the units are N/m. The positive sign of this force means that the moving dissociated <a> dislocation suffers a repulse force when it moves close to the adjacent SFs. The maximum repelling force is inversely proportional to the spacing distance between adjacent SFs, which means introducing a high density of SFs can effectively impede the motion of dislocations on the basal plane. Therefore, the Mg-8.5Gd-2.3Y-1.8Ag-0.4Zr (wt.%) alloy can be strengthened by tailoring the microstructure with high density of SFs.

Fig.5.3 (a) and (b) show the other type of configuration of interaction between dissociated <a>

dislocation on basal plane and SFs. The only difference between Fig.5.1 and Fig. 5.2 is that

$\bar{b}_6$  will encounter and interact with the adjacent SFs.  $\bar{b}_1 = \bar{b}_3 = b_{1e}i + b_{1s}k$  and

$\bar{b}_6 = b_{6e}i + b_{6s}k = b_{1e}i - b_{1s}k$ , where  $b_{1e} = \frac{\sqrt{3}}{2}b_1$  and  $b_{1s} = -\frac{1}{2}b_1$  are the magnitude of the edge

and screw component of  $\bar{b}_1$ . The stress of dislocation  $\bar{b}_1$  on dislocation  $\bar{b}_6$  is:

$$\bar{\sigma}_{16} = ii\sigma_{xx} + ij\sigma_{xy} + ji\sigma_{yx} + jj\sigma_{yy} + kk\sigma_{zz} + ik\sigma_{xz} + ki\sigma_{zx} + jk\sigma_{yz} + kj\sigma_{zy} \quad (5.7)$$

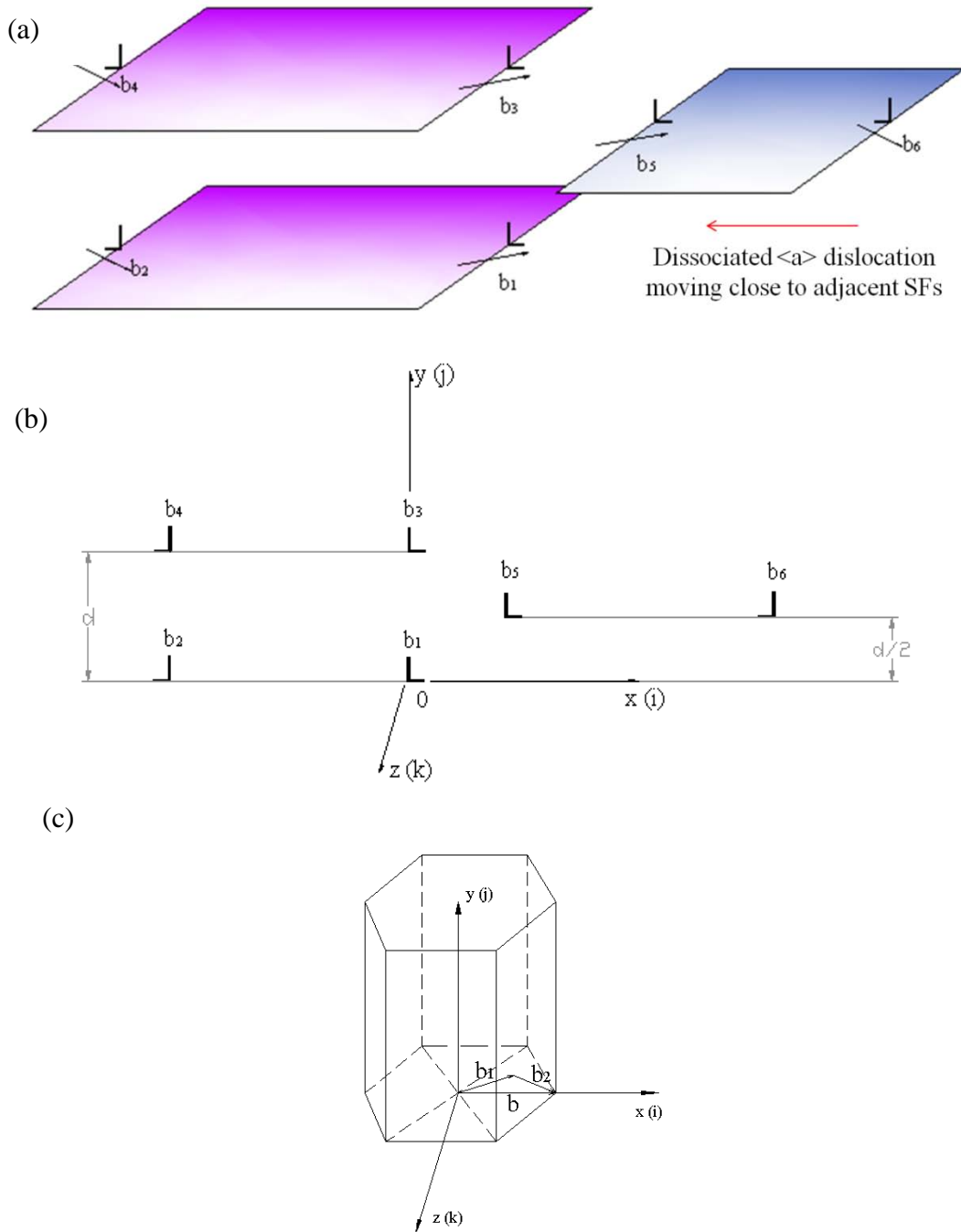


**Figure 5.2** Schematic illustration of (a) the interaction of  $\langle a \rangle$  dislocation with two adjacent stacking faults, (b) and (c) show how to establish the co-ordinate system for stress calculation using Peach-Koehler equation.

From the Peach-Koehler formula, the force exerted on a unit length of dislocation  $\bar{b}_6$  due to the stress field of dislocation  $\bar{b}_1$  is  $\bar{F}_{16} = (\bar{\sigma}_{16} \cdot \bar{b}_6) \times \bar{\xi}_6$ . Substituting the  $\bar{\sigma}_{15}$  and  $\bar{b}_5$ , so

$$\begin{aligned} \bar{\sigma}_{16} \cdot \bar{b}_6 &= (ii\sigma_{xx} + ij\sigma_{xy} + ji\sigma_{yx} + jj\sigma_{yy} + kk\sigma_{zz} + ik\sigma_{xz} + ki\sigma_{zx} + jk\sigma_{yz} + kj\sigma_{zy}) \cdot (b_{1e}i - b_{1s}k) \\ &= (\sigma_{xx}b_{1e} - \sigma_{xz}b_{1s})i + (\sigma_{yx}b_{1e} - \sigma_{yz}b_{1s})j + (\sigma_{zx}b_{1e} - \sigma_{zz}b_{1s})k \end{aligned} \quad (5.8)$$

$$\begin{aligned} \bar{F}_{16} &= (\bar{\sigma}_{16} \cdot \bar{b}_6) \times \bar{\xi}_6 = [(\sigma_{xx}b_{1e} - \sigma_{xz}b_{1s})i + (\sigma_{yx}b_{1e} - \sigma_{yz}b_{1s})j + (\sigma_{zx}b_{1e} - \sigma_{zz}b_{1s})k] \times k \\ &= (\sigma_{yx}b_{1e} - \sigma_{yz}b_{1s})i - (\sigma_{xx}b_{1e} - \sigma_{xz}b_{1s})j \end{aligned} \quad (5.9)$$

Therefore the force exerted on a unit length of dislocation  $\bar{b}_6$  due to the stress field of dislocation  $\bar{b}_1$  along x(i) direction is

$$\begin{aligned} F_{16}|_i &= \sigma_{yx}b_{1e} - \sigma_{yz}b_{1s} = \frac{\mu b_{1e}}{2\pi(1-\nu)} \frac{x(x^2 - y^2)}{(x^2 + y^2)^2} b_{1e} - \frac{\mu b_{1s}}{2\pi} \frac{x}{x^2 + y^2} b_{1s} \\ &= \frac{\mu \frac{\sqrt{3}}{2} b_1}{2\pi(1-\nu)} \frac{x(x^2 - y^2)}{(x^2 + y^2)^2} \frac{\sqrt{3}}{2} b_1 - \frac{\mu(-\frac{1}{2})b_1}{2\pi} \frac{x}{x^2 + y^2} (-\frac{1}{2})b_1 \\ &= \frac{3\mu b_1^2}{8\pi(1-\nu)} \frac{x(x^2 - y^2)}{(x^2 + y^2)^2} - \frac{\mu b_1^2}{8\pi} \frac{x}{x^2 + y^2} \end{aligned} \quad (5.10)$$

The same derivation procedure can be applied to obtain the force exerted on a unit length of dislocation  $\bar{b}_6$  due to the stress field of dislocation  $\bar{b}_3$  along x(i) direction is

$$F_{36}|_i = \sigma_{yx}b_{3e} - \sigma_{yz}b_{3s} = \frac{3\mu b_1^2}{8\pi(1-\nu)} \frac{x[x^2 - (y-d)^2]}{[x^2 + (y-d)^2]^2} - \frac{\mu b_1^2}{8\pi} \frac{x}{x^2 + (y-d)^2} \quad (5.11)$$

Therefore the total force exerted on a unit length of dislocation  $\bar{b}_6$  due to the stress field of dislocation  $\bar{b}_1$  and  $\bar{b}_3$  along x(i) direction is

$$F_{total}|_i = F_{16}|_i + F_{36}|_i = \frac{3\mu b_1^2}{8\pi(1-\nu)} \frac{x(x^2 - y^2)}{(x^2 + y^2)^2} - \frac{\mu b_1^2}{8\pi} \frac{x}{x^2 + y^2} + \frac{3\mu b_1^2}{8\pi(1-\nu)} \frac{x[x^2 - (y-d)^2]}{[x^2 + (y-d)^2]^2} - \frac{\mu b_1^2}{8\pi} \frac{x}{x^2 + (y-d)^2} \quad (5.12)$$

Because the dissociated  $\langle a \rangle$  dislocation moves on the basal plane which is equal in spacing distance,  $d/2$ , from each SF,  $y=d/2$  can be substituted in  $F_{total}|_i$ .

$$F_{total}|_i = \frac{3\mu b_1^2}{4\pi(1-\nu)} \frac{x(x^2 - \frac{1}{4}d^2)}{(x^2 + \frac{1}{4}d^2)^2} - \frac{\mu b_1^2}{4\pi} \frac{x}{x^2 + \frac{1}{4}d^2} \quad (5.13)$$

where  $\mu=18.07$  GPa is the shear modulus[15],  $b_1 = \frac{\sqrt{3}}{3}a = 0.1853 \times 10^{-9} m$ , Poisson's ratio

$\gamma=0.35$ [16]. By resolving the above equation,  $F_{total}|_i = -0.1502 \frac{1}{d}$  was obtained with unit in

N/m. The negative sign of  $F_{total}|_i$  means the maximum interaction force between SFs and dislocations of this type of configuration is an attractive force. The interaction force between the SF and dislocation is again inversely proportional to the spacing distance of the adjacent SFs which means the materials can be strengthened by introducing high density of SFs.

#### 5.4 $\langle c \rangle$ Dislocation and $\langle c+a \rangle$ Dislocation Interact with SFs

In Mg alloy, the  $\langle c+a \rangle$  dislocation,  $\frac{1}{3}\langle 11\bar{2}3 \rangle$ , usually slips on the pyramidal plane,  $\{11\bar{2}2\}$ . Fig. 5.4 shows the  $\langle c+a \rangle$  dislocation,  $\frac{1}{3}[1\bar{2}13]$ , slipping on the pyramidal plane,  $(\bar{1}2\bar{1}2)$ . From the crystallographic point of view, a  $\langle c+a \rangle$  dislocation can be decomposed into a  $\langle a \rangle$  dislocation slipping on the basal plane plus a  $\langle c \rangle$  dislocation slipping on the

prismatic plane. Therefore, the interaction force between <c+a> dislocation and SFs can be summed by the interaction force of <a> dislocation vs. SFs and <c> dislocation vs. SFs. As calculated in the previous sections, the interaction force between <a> dislocation and SFs is proportional to the reciprocal of the average spacing between adjacent SFs. Here, we will calculate the interaction force of <c> dislocations vs. SFs.

Fig. 5.5 shows the configuration of the adjacent SFs bounded by two pairs of partial dislocations,  $\bar{b}_1$  and  $\bar{b}_2$  and  $\bar{b}_3$  and  $\bar{b}_4$ , and a <c> dislocation,  $\bar{b}_5$ . The stress of dislocation  $\bar{b}_1$  on dislocation  $\bar{b}_5$  is

$$\bar{\sigma}_{15} = i i \sigma_{xx} + i j \sigma_{xy} + j i \sigma_{yx} + j j \sigma_{yy} + k k \sigma_{zz} + i k \sigma_{xz} + k i \sigma_{zx} + j k \sigma_{yz} + k j \sigma_{zy} \quad (5.14)$$

From the Peach-Koehler formula, the force exerted on a unit length of dislocation  $\bar{b}_5$  due to the stress field of dislocation  $\bar{b}_1$  is  $\bar{F}_{15} = (\bar{\sigma}_{15} \cdot \bar{b}_5) \times \bar{\xi}_5$ , where  $\bar{\xi}_5 = k$  is the sense vector of the <c> dislocation. Substituting the  $\bar{\sigma}_{15}$  and  $\bar{b}_5$ ,

$$\bar{F}_{15} = (\bar{\sigma}_{15} \cdot \bar{b}_5) \times \bar{\xi}_5 = -\sigma_{yy} b_5 i + \sigma_{xy} b_5 j \quad (5.15)$$

Therefore the force exerted on a unit length of dislocation  $\bar{b}_5$  due to the stress field of dislocation  $\bar{b}_1$  along y(j) direction is

$$F_{15}|_j = \sigma_{xy} b_5 = \frac{\mu b_1}{2\pi(1-\nu)} \frac{x(x^2 - y^2)}{(x^2 + y^2)^2} b_5 \quad (5.16)$$

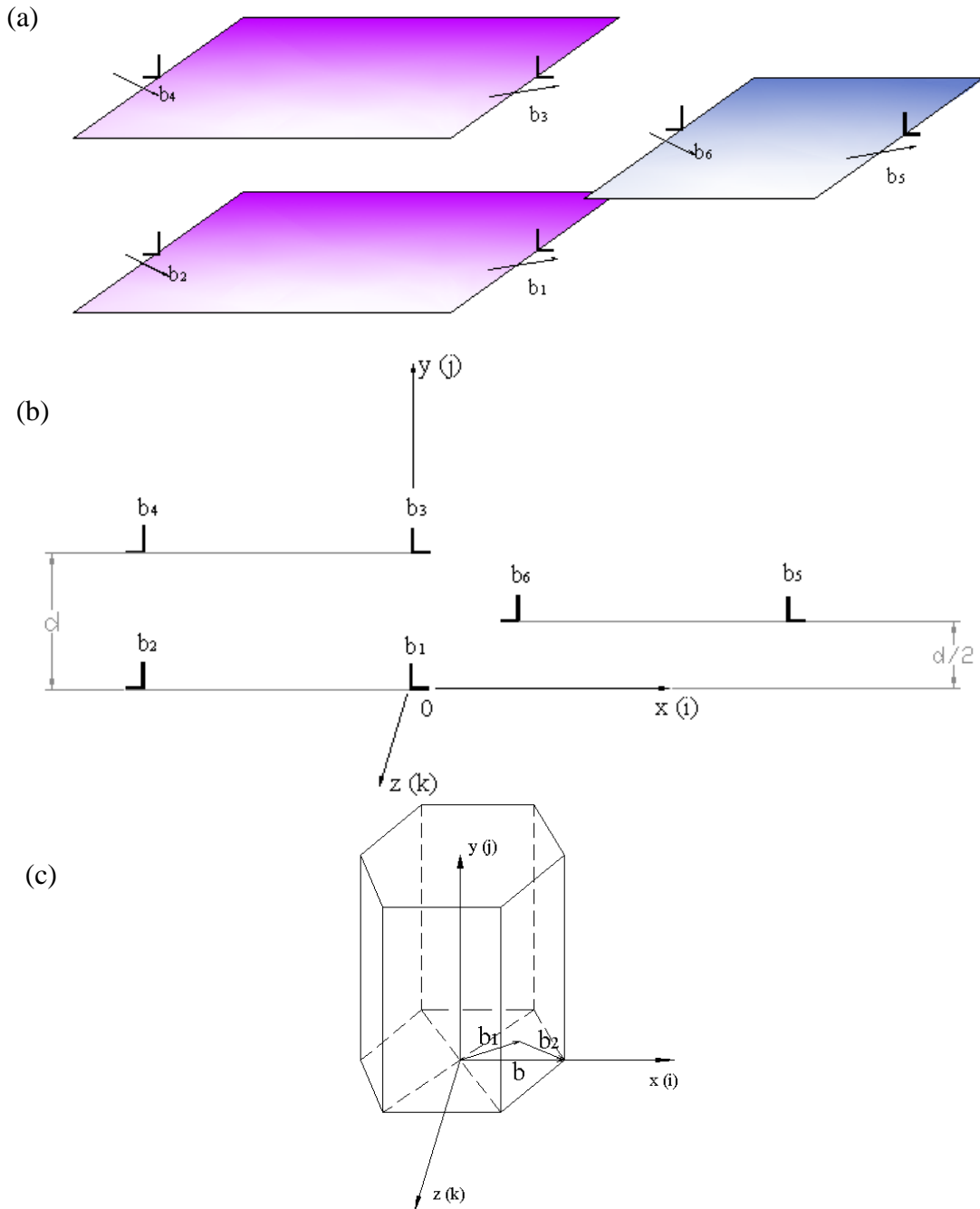


**Figure 5.3** Schematic illustration of (a) the interaction of  $\langle a \rangle$  dislocation with two adjacent stacking faults, (b) and (c) show how to establish the co-ordinate system for stress calculation using Peach-Koehler equation.

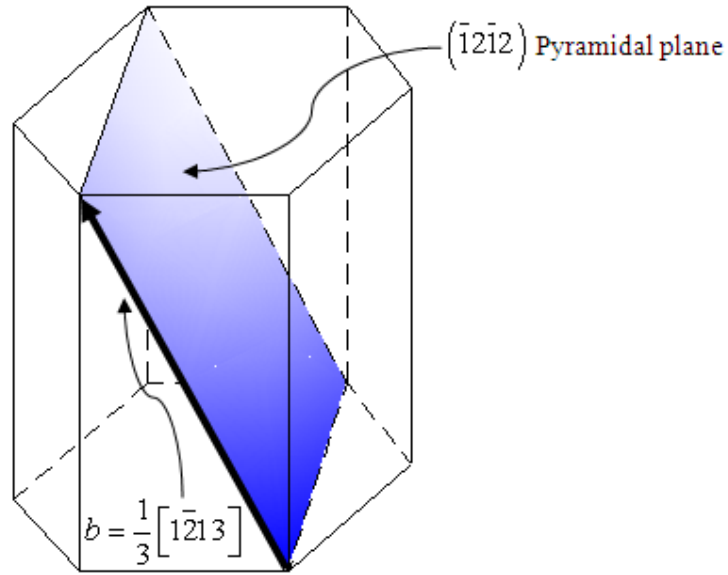


**Figure 5.4** Schematic illustration of non basal slip system.

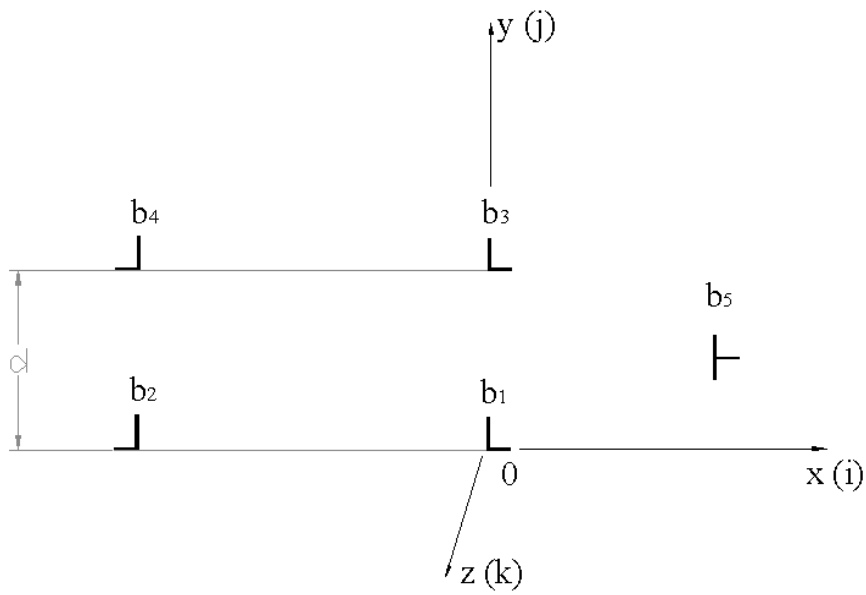


**Figure 5.5** Configuration of the  $\langle c \rangle$  dislocation interact with two adjacent SFs.

The same derivation procedure can be applied to obtain the force exerting on unit length of dislocation  $\bar{b}_5$  due to the stress field of dislocation  $\bar{b}_3$  along y(j) direction is

$$F_{35}|_j = \sigma_{xy} b_5 = \frac{\mu b_3}{2\pi(1-\nu)} \frac{x[x^2 - (y-d)^2]}{[x^2 + (y-d)^2]^2} b_5 \quad (5.17)$$

Therefore the total force exerted on a unit length of dislocation  $\bar{b}_5$  due to the stress field of dislocation  $\bar{b}_1$  and  $\bar{b}_3$  along y(j) direction is

$$F_{total}|_j = F_{15}|_j + F_{35}|_j = \frac{\mu b_1}{2\pi(1-\nu)} \frac{x(x^2 - y^2)}{(x^2 + y^2)^2} b_5 + \frac{\mu b_3}{2\pi(1-\nu)} \frac{x[x^2 - (y-d)^2]}{[x^2 + (y-d)^2]^2} b_5 \quad (5.18)$$

In this equation, there are two variables, x and y, which are the coordinates of the position of <c> dislocation. Because the slip plane of <c> dislocation is the prismatic plane which is perpendicular to basal plane, x value is no longer a variable once the <c> dislocation nucleates and starts to move. Therefore, we assume that x value of the position of <c> dislocation is fixed and proportional to the average spacing, d, between SFs. Table 5.1 gives the maximum interaction force between <c> dislocation and SFs at a few selected x values.

The above calculation demonstrated that the maximum interaction force between <c> dislocation and SFs is also proportional to the reciprocal of the average spacing of adjacent SFs, d. Therefore, the maximum interaction force between <c+a> dislocation and SFs is also proportional to the reciprocal of the average spacing of adjacent SFs, d.

There are also possibilities that a <c+a> dislocation moves closer to a SF and then cut through the SF and leaves a step on the SF as shown in Fig. 5.6. The applied force needed for a non basal dislocation to move on the slip plane can be expressed as  $F = \tau_f b t$ , where  $\tau_f$  is the flow stress needed for a non basal dislocation to move on the slip plane, b is the Burger vector of non basal dislocation and t is the length of dislocation. Here we assume  $E_{CSF}$  is the

energy for a dislocation with unit length to cut through a SF. The energy for a dislocation to cut through one SF is

$$E = F \cdot \frac{d}{\sin \theta} + E_{CSF} \cdot t \quad (5.19)$$

**Table 5.1** Maximum interaction force between <c> dislocation and SFs at few selected x Values.

	x=4d	x=2d	x=d	x=0.75d	x=0.5d	x=0.25d
<i>Max. F<sub>total</sub></i>	0.2040·d <sup>-1</sup>	0.3549·d <sup>-1</sup>	0.4400·d <sup>-1</sup>	0.5137·d <sup>-1</sup>	3.5280·d <sup>-1</sup>	6.7497·d <sup>-1</sup>
(N/m)						

**Table 5.1** Continued

	x=-0.25d	x=-0.5d	x=-0.75d	x=-d	x=-2d
<i>Max. F<sub>total</sub></i>	-1.6209·d <sup>-1</sup>	-0.7522·d <sup>-1</sup>	-0.5137·d <sup>-1</sup>	-0.4400·d <sup>-1</sup>	-0.3549·d <sup>-1</sup>
(N/m)					

If the moving distance of a dislocation is x, so the number of SFs which are cut by this dislocation will be  $n = \frac{x}{d / \sin \theta}$ , where  $\theta$  is the acute angle between the normal directions of basal plane and slip plane as shown in Fig. 5.6 a. So the total energy needed for a dislocation to cut “n” SFs will be:

$$E(x) = E \cdot n = \left( \tau_f b t \frac{d}{\sin \theta} + E_{CSF} t \right) \frac{x}{d / \sin \theta} \quad (5.20)$$

The applied force needed for a dislocation to move and cut the SFs can be the differential of the energy with respect to the working distance, which is:

$$F = \frac{dE(x)}{dx} = \tau_f b t + \frac{E_{CSF} t \sin \theta}{d} \quad (5.21)$$

Therefore, the applied force per unit length of dislocation is:

$$\frac{F}{t} = \tau_f b + \frac{E_{CSF} \sin \theta}{d} \quad (5.22)$$

The applied stress per unit length of dislocation for a dislocation to cut through a SF will be:

$$\tau_{app} = \frac{F}{t \cdot b} = \tau_f + \frac{E_{CSF} \sin \theta}{b \cdot d} \quad (5.23)$$

Thus the applied stress needed for a non basal dislocation to move and cut through SFs is proportional to 1/d, where d is the mean spacing between adjacent SF. This applied force can be barriers for dislocations to move. Therefore, as the density of SFs increased, there will be more barriers for dislocations to overcome in order to move and the strength of the Mg alloy was increased.

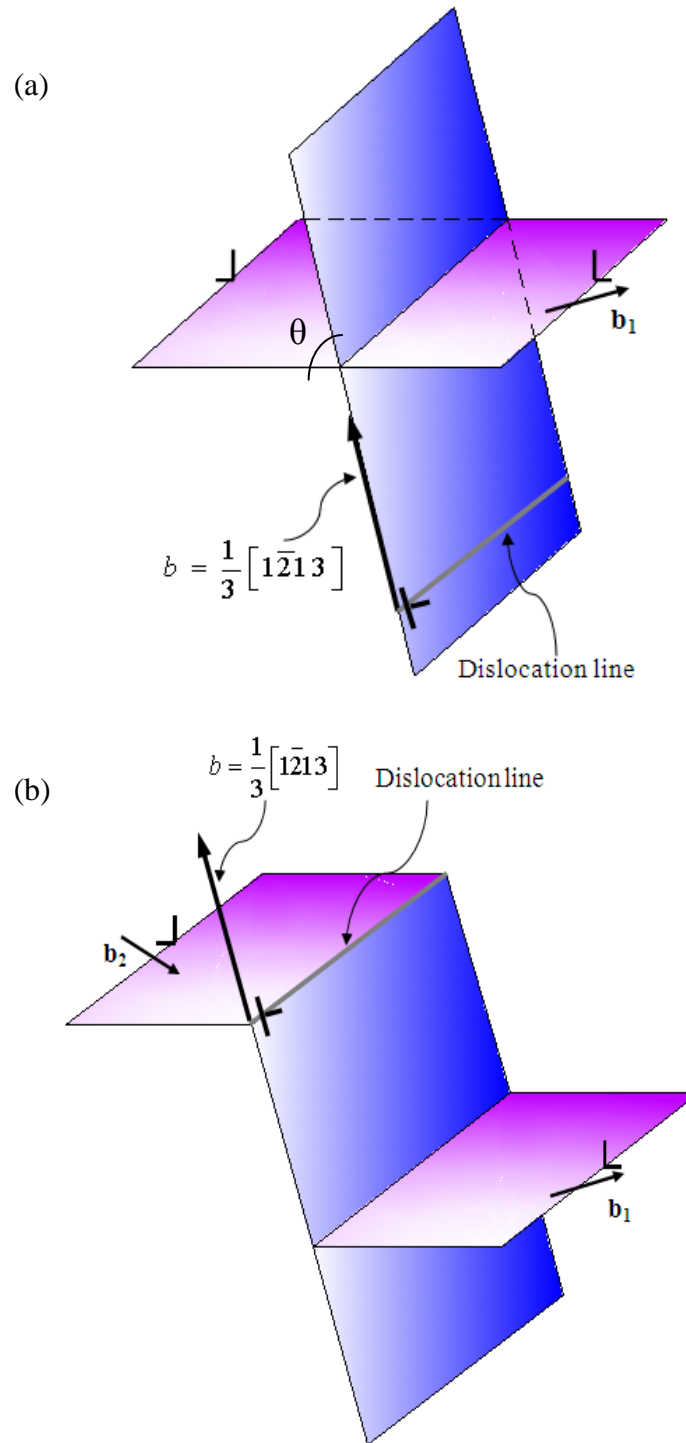


**Figure 5.6** Schematical illustration for (a)  $\langle c+a \rangle$  dislocation moves close to a stacking fault and (b)  $\langle c+a \rangle$  dislocation cut through a SF and leave a step on the SF.

## 5.5 Summary

The model of interactions between basal SFs and basal  $\langle a \rangle$  dislocations and non basal  $\langle c+a \rangle$  dislocations were established for the first time in Mg alloy. The model shows that the strengthening is proportional to the reciprocal of the SF spacing for both types of interactions between dislocations and SFs. Therefore, decreasing the SF spacing can increase interaction force which serve as a barrier for a dislocation to move, and consequently improve the macroscopic strength of materials.

In this research, we only consider the scenarios based on assumption that all the SFs and partial dislocations are formed by dissociation of the full edge dislocations. In the real cases, the situations might be more complicated than our assumption since the screw dislocations and mixed dislocations might also activate during tensile tests. We are now attempting to develop more comprehensive models to better analyze the interaction force between SFs and various types of dislocations in hcp Mg alloy.

## REFERENCES

- [1] Sarma VS, Wang J, Jian WW, Kauffmann A, Conrad H, Freudenberger J, et al. Role of stacking fault energy in strengthening due to cryo-deformation of FCC metals. *Materials Science and Engineering A* 2010;527:7624-30.
- [2] Bahmanpour H, Kauffmann A, Khoshkhoo MS, Youssef KM, Mula S, Freudenberger J, et al. Effect of stacking fault energy on deformation behavior of cryo-rolled copper and copper alloys. *Materials Science and Engineering A* 2011;529:230-6.
- [3] Youssef K, Sakaliyska M, Bahmanpour H, Scattergood R, Koch C. Effect of stacking fault energy on mechanical behavior of bulk nanocrystalline Cu and Cu alloys. *Acta Materialia* 2011;59:5758-64.
- [4] Zhao YH, Zhu YT, Liao XZ, Horita Z, Langdon TG. Tailoring stacking fault energy for high ductility and high strength in ultrafine grained Cu and its alloy. *Applied Physics Letters* 2006;89.
- [5] Sandlobes S, Friak M, Zaefferer S, Dick A, Yi S, Letzig D, et al. The relation between ductility and stacking fault energies in Mg and Mg-Y alloys. *Acta Materialia* 2012;60:3011-21.
- [6] Peach M, Koehler JS. The forces exerted on dislocations and the stress fields produced by them. *Physical Review* 1950;80:436-9.
- [7] Lu L, Chen X, Huang X, Lu K. Revealing the maximum strength in nanotwinned copper. *Science* 2009;323:607-10.
- [8] Dao M, Lu L, Shen YF, Suresh S. Strength, strain-rate sensitivity and ductility of copper with nanoscale twins. *Acta Materialia* 2006;54:5421-32.

- [9] Lu K, Lu L, Suresh S. Strengthening materials by engineering coherent internal boundaries at the nanoscale. *Science* 2009;324:349-52.
- [10] Zhu T, Li J, Samanta A, Kim HG, Suresh S. Interfacial plasticity governs strain rate sensitivity and ductility in nanostructured metals. *Proceedings of the National Academy of Sciences* 2007;104:3031-6.
- [11] Agnew S, Horton J, Yoo M. Transmission electron microscopy investigation of  $\langle c+a \rangle$  dislocations in Mg and  $\alpha$ -solid solution Mg-Li alloys. *Metallurgical and Materials Transactions A* 2002;33:851-8.
- [12] Li B, Yan PF, Sui ML, Ma E. Transmission electron microscopy study of stacking faults and their interaction with pyramidal dislocations in deformed Mg. *Acta Materialia* 2010;58:173-9.
- [13] Agnew SR, Duygulu Ö. Plastic anisotropy and the role of non-basal slip in magnesium alloy AZ31B. *Int J Plasticity* 2005;21:1161-93.
- [14] Zhu YT, Wu XL, Liao XZ, Narayan J, Kecskés LJ, Mathaudhu SN. Dislocation–twin interactions in nanocrystalline fcc metals. *Acta Materialia* 2011;59:812-21.
- [15] Wang QD. Unpublished data.
- [16] Zheng L, Liu C, Wan Y, Yang P, Shu X. Microstructures and mechanical properties of Mg–10Gd–6Y–2Zn–0.6Zr(wt.%) alloy. *J Alloy Compd* 2011;509:8832-9.

## CHAPTER 6: Conclusions and Future work

### 6.1 Conclusions

Magnesium and its alloys have attracted extensive attention in recent years due to their abundance, low-density, good castability and recyclability. In this research, we processed a Mg-8.5Gd-2.3Y-1.8Ag-0.4Zr (wt.%) via conventional technique (hot-rolling at 450°C) with thickness reduction up to 88%. The following are a collection of outcomes and conclusions made over the course of this work:

Firstly, we reported a new mechanism for producing ultrahigh strengths (yield strength: ~575 MPa, ultimate strength: ~600 MPa) and maintaining moderate ductility (uniform elongation: ~5.2 %) in hot rolled Mg-alloy with relatively large grain sizes (13  $\mu\text{m}$ ). TEM observations shown that a high density of nano-spaced SFs were the main defects inside of the grains and their density increased as rolling thickness reduction increased. The strength of the processed Mg alloy was found to increase as the mean spacing between adjacent SFs decreased. Nano-spaced SFs are found to be very effective in impeding the movement of dislocations and retaining strain hardening. Activation of non-basal dislocations during tensile testing accounts for the detected moderate ductility, in addition to the capability of retaining strain hardening.

Secondly, we predicted and calculated contributions from different strengthening mechanisms for the unltrahigh strength of hot rolled Mg alloy including solid solution, grain refinement, precipitation and texture evolution. The results showed that grain boundary strengthening, solid solution hardening, precipitates hardening and strong texture strengthening totally contribute 249.8 MPa to 278.5 MPa for the yield strength (~575MPa) of

88% rolled Mg alloy. In other words, the nano-spaced SFs strengthening mechanism was the main strengthening factor, which solely contributed 326.2 MPa to 296.5 MPa, around 50% of the total yield strength.

Finally, the model of interactions between basal SFs and basal  $\langle a \rangle$  dislocations and non basal  $\langle c+a \rangle$  dislocations were established for the first time in Mg alloy. The model shows that the strengthening is proportional to the reciprocal of the SF spacing for both types of interactions between dislocations and SFs. Therefore, decreasing the SF spacing can increase interaction force which serve as a barrier for a dislocation to move, and consequently improve the macroscopic strength of materials.

## 6.2 Future Work

In this research, we report a new mechanism for inducing ultrahigh strengths (yield strength: ~575 MPa, ultimate strength: ~600 MPa) and maintaining moderate ductility (uniform elongation: ~5.2 %) via conventional processing (hot-rolling) of a Mg-alloy (Mg-8.5Gd-2.3Y-1.8Ag-0.4Zr (wt.%)) with relatively large grain sizes (13  $\mu\text{m}$ ). Nano-spaced SFs are found to be very effective in impeding the movement of dislocation and retaining strain hardening. This strengthening mechanism provides a new strategy to increase the strength without severe loss of the ductility. In the future, our research work will include:

- (1) Investigate the microstructure evolution and SFs formation mechanism in hot rolled Mg alloy.
- (2) Optimize the rolling parameters and explore the possibility to further improve mechanical property.
- (3) Develop new Mg-RE alloy with low content of RE elements, which can be processed

by conventional techniques and also can yield excellent mechanical property.

(4) Transfer the Nano-Spaced SFs strengthening mechanism to fcc metals.

## APPENDIX

## Appendix A: Solution Treatment

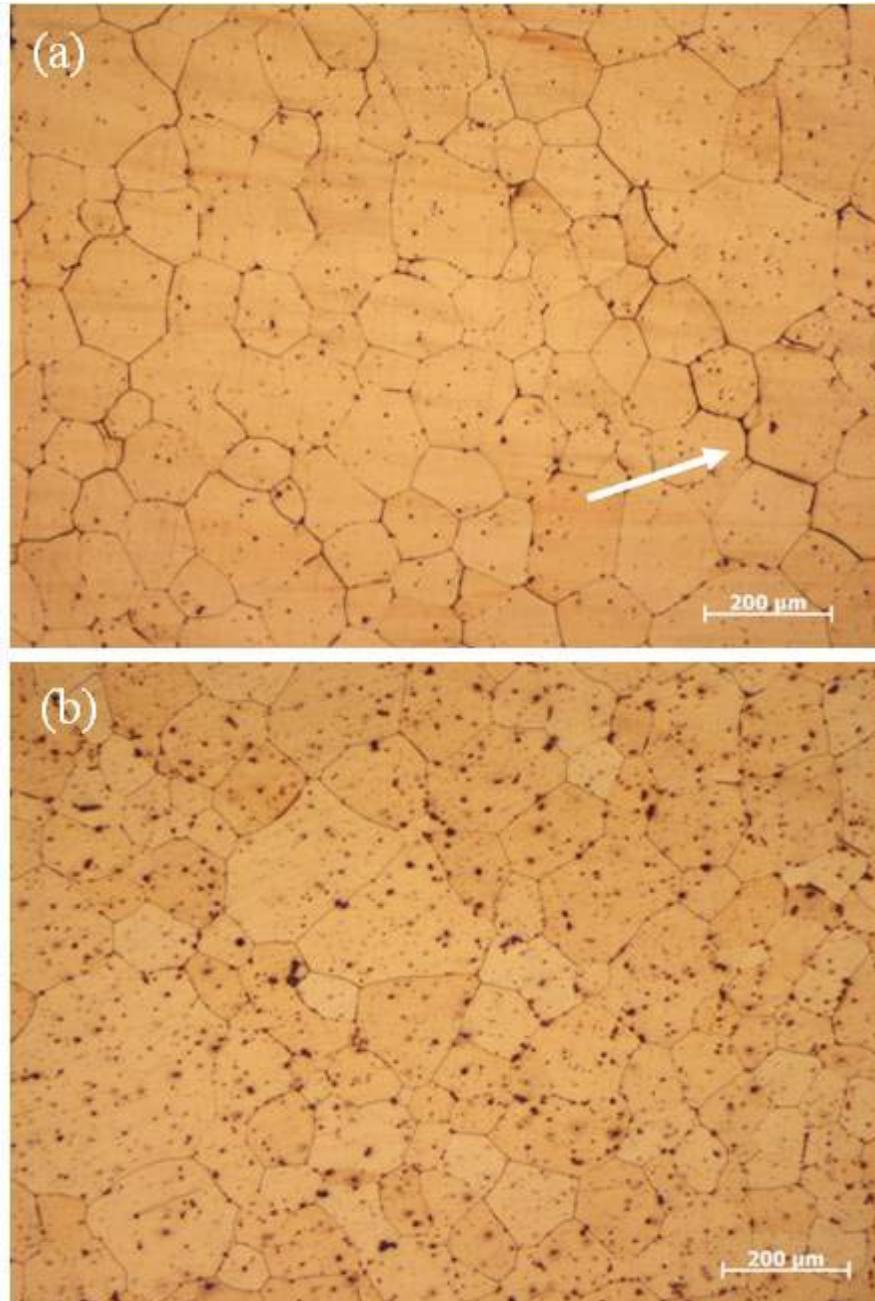
As indicated in the references [20] in Chapter 3, the solution treatment for Mg-Gd-Y-Zr alloy can be conducted at the temperature ranging from 500°C to 520°C for ~ 10 hours and then the samples was quenched in room temperature water. In this research, the samples for the solution treatment were sealed in quartz, vacuumed by a mechanical pump and heated by a digital-controlled furnace. After solution treated in the furnace, the quartz was vented by pure argon and then samples were immediately quenched in quenching media

As shown in Fig.A.1 (a), the solution treatment at 520 °C for 10 hours was able to dissolve most precipitates into Mg matrix. However room water quenching introduced some cracks propagating from the edge to the center of the samples, as indicated by the white arrow in Fig. A.1(a). The quenching cracks can be found on all the samples with different dimensions.

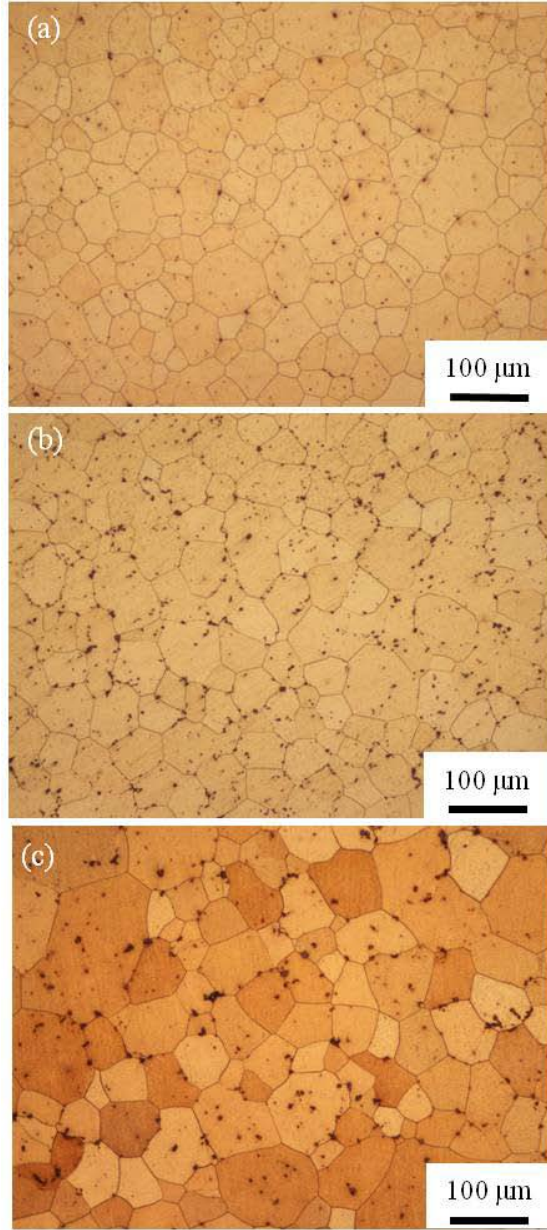
In order to slow down the cooling rate of quenching media to prevent quenching cracks on the sample, engine oil was used. The quenched samples were free of cracks but OM image in Fig.A.1 (b) shown that the second phases precipitated on grain boundaries and grain interior during quenching. It was also found in Fig. A.1 (b) that the grains obviously grown to ~200  $\mu\text{m}$  which was five times as large as the grain size of as-cast sample. So here we have two conclusions: (1) the cooling rate of engine oil was too slow to keep most of precipitates in the Mg matrix during quenching and (2) heating at 520 °C for 10 hours was not an appropriate solution treatment parameter since the grain grown obviously.

Fig. A.2 shows the OM images of samples solution treated at 500 °C for 10 hours and then quenched in room temperature water. As shown in Fig. A.2 (a), most of the grain

boundaries were free from precipitates. However there were cracks on the sample (not shown in Fig. A.2) with a relatively large dimension, such as  $\sim 12 \text{ mm} \times 12 \text{ mm} \times 6 \text{ mm}$ . The grain size of the sample solution treated at  $500 \text{ }^\circ\text{C}$  for 10 hours was  $\sim 50 \text{ }\mu\text{m}$ . In order to prevent quenching cracks, three solution treated samples with different dimensions were then quenched in room temperature silicon oil. All the samples were survived from any quenching cracks but there were lots of precipitates existing around the grain boundaries in Fig. A.2(b). Prolonging the solution time to 12 hours, the density of precipitates on the grain boundaries or within grains became much less than those in samples solution treated for 10 hours, as seen in Fig. A.2(c). The grain size of samples solution treated at  $500 \text{ }^\circ\text{C}$  for 12 hours was about  $\sim 61 \mu\text{m}$  which was acceptable compared with the grain size of as-cast samples,  $\sim 40 \mu\text{m}$ .



**Figure A.1** OM images of Mg-8.5Gd-2.3Y-2.0Ag-0.4Zr alloy solution treated at 520 °C for 10 hours and then quenched in different media: (a) 20 °C water, (b) engine oil.



**Figure A.2** OM images of Mg-8.5Gd-2.3Y-2.0Ag-0.4Zr alloy solution treated at different temperatures for variant time and then quenched in different media: (a) 500 °C for 10 hours, quenched in 20 °C water, (b) 500 °C for 10 hours, quenched in room temperature silicon oil and (c) 500 °C for 12 hours, quenched in room temperature silicon oil.

## Appendix B: Calculations of the Diameter and Volume Fraction of Precipitates

In order to calculate the Orowan stress for dislocation to by-pass the precipitates using equation 4.3, the volume fraction and mean diameter of the precipitates should be known. As shown in Fig. A.3, all precipitates, except for # 19, 20 and 21, could be approximately regarded as spherical particles. Processing this TEM image using professional software, the image pixels of individual precipitates can be obtained as shown in Table 1. The total pixels of 18 precipitates are 102614. The pixel of the image is  $1819 \times 1674 = 3045006$ . So the area fraction of the precipitates is  $102614/3045006 = 0.0337$ .

According to the reference [11] in chapter 4, the volume fraction of precipitates,  $f_v = N_a \cdot S_p$ , where  $S_p$  is the mean planer cross-sectional area of each single particle and  $N_a$  is the number of particles intersected per unit area of slip plane. We assume that the area of this TEM image is  $S_{image}$ . Since the electron beam of TEM observation is perpendicular to the rolling plane which is parallel to the basal plane of 88% rolled sample (strong basal texture with basal plane parallel to rolling plane), the area of slip plane intersected with these 18 precipitates is equal to  $S_{image}$ .

$$\text{Therefore, } S_p = \frac{0.0337 \cdot A}{18}, N_a = \frac{18}{S_{image}} \text{ and } f_v = N_a \cdot S_p = \frac{18}{S_{image}} \cdot \frac{0.0337 \cdot S_{image}}{18} = 0.0337.$$

In equation 4.3,  $d$  is the mean diameter of the precipitates. We assume this diameter has image pixels of  $P_d$ . The mean radius of the 18 precipitates in pixels can be calculated by

$$18\pi r^2 = 102614. \text{ Therefore the diameter in pixels } P_d = \sqrt{\frac{102614}{18\pi}} \cdot 2 = 85.22.$$

Since the scale bar is  $4 \mu\text{m}$  which is equal to 355 pixels in the Fig. A.3, the mean diameter of the precipitates

$d = \frac{85.22}{355} \cdot 4 = 0.96 \mu\text{m}$ . Once the volume fraction and mean diameter of precipitates were obtained, the precipitates hardening contribution can be calculated as shown in section 4.2.3 of chapter 4.

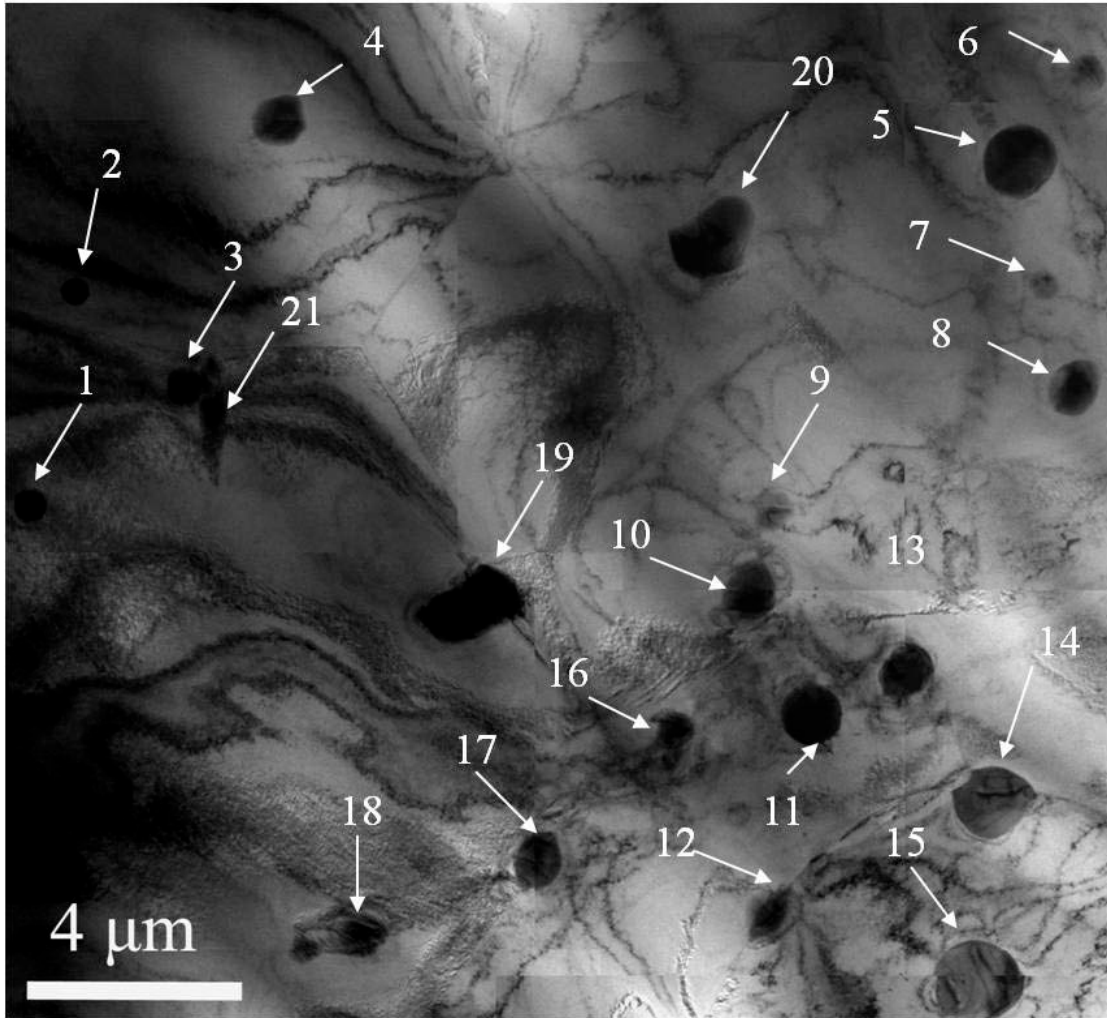


**Figure A.3** The typical precipitates in 88% rolled Mg-8.5Gd-2.3Y-1.8Ag-0.4Zr (wt.%) alloy samples.

**Table A.1** The image pixels of 18 precipitates in Figure A.3.

Precipitate #	pixels	Precipitate #	pixels	Precipitate #	pixels
1	2218	7	1703	13	6832
2	1464	8	6140	14	11599
3	2276	9	1617	15	15487
4	5796	10	6931	16	3060
5	11196	11	8011	17	6094
6	2782	12	4356	18	5052